MNRAS **000**, 1–13 (2017) Preprint 5 September 2018 Compiled using MNRAS LATEX style file v3.0

A search for hypercompact HII regions in the Galactic Plane

A. Y. Yang,[1,2,3,6] M. A. Thompson,[3] W.W. Tian,[1,2,5] S. Bihr,[4] H. Beuther[4], L. Hindson[3]
[1] *Key Laboratory of Optical Astronomy, National Astronomical Observatories, Chinese Academy of Sciences, Beijing 100012, China*
[2] *University of Chinese Academy of Sciences, 19A Yuquan Road, Beijing 100049, China*
[3] *Centre for Astrophysics Research, School of Physics Astronomy & Mathematics, University of Hertfordshire, College Lane, Hatfield, AL10 9AB, U*
[4] *Max-Planck Institute for Astronomy, Königstuhl 17, 69117 Heidelberg, Germany*
[5] *Department of Physics & Astronomy, University of Calgary, Alberta t1N 1N4, Canada*
[6] *Max Planck Institute for Radio Astronomy, Auf dem Hügel 69, 53121, Bonn, Germany*

Accepted XXX. Received YYY; in original form ZZZ

ABSTRACT

We have carried out the largest and most unbiased search for hypercompact (HC) HII regions. Our method combines four interferometric radio continuum surveys (THOR, CORNISH, MAGPIS and White2005) with far-infrared and sub-mm Galactic Plane surveys (Hi−GAL and ATLASGAL) to identify embedded HII regions with positive spectral indices. Of a total sample of 534 radio sources with positive spectral indices, we have identified 120 positive spectra HII regions embedded within molecular cloud clumps. None of these HII regions fulfills the canonical definition of an HC HII region at 5 GHz. We suggest that HC HII regions have a hierarchical structure of ionized gas that results in an extended morphology at 5 GHz. Examining known ultracompact (UC) HII region surveys, we find that roughly half of those detected have positive spectral indices. These rising spectra HII regions are statistically more luminous and possess higher Lyman continuum fluxes than HII regions with flat or negative indices (i.e., not-rising). We see no differences in clump mass, linear diameter or luminosity-to-mass ratio between rising spectrum and not-rising spectrum HII regions.

Key words: ISM: HII regions – radio continuum: ISM – infrared: ISM –submillimetre: ISM

1 INTRODUCTION

Newly formed massive stars are deeply embedded within molecular clouds, but they produce powerful Lyman continuum emission that is sufficiently energetic to ionize their surroundings and create observable ionized regions, known as HII regions. HII regions are over-pressured with respect to the surrounding interstellar medium and so expand over time, driving ionization shocks into the ambient medium (Tenorio-Tagle 1979; Dyson et al. 1995). The smallest HII regions are thus likely to be the youngest, which means that the most dense and compact HII regions can shed light on the early development of massive stars (Peters et al. 2010).

However, many details involved in these early stages are currently unclear (Hoare et al. 2007; Zinnecker & Yorke 2007), and different theoretical models predict very different outcomes in the earliest stages of HII regions. For example, as massive stars reach the main sequence while still accreting material, the McKee & Tan (2003) and Peters et al. (2010) turbulent core and ionization feedback models both envisage the youngest HII regions expanding into outflow-driven cavities (e.g. Tan & McKee 2003; Tanaka et al. 2016) away from the main accretion flows, indicating that they are expected to develop early. But in the model of Hosokawa & Omukai (2009) and Hosokawa et al. (2010), the high accretion rates cause the outer layers of the youngest massive stars to swell, delaying the initial development of HII regions until the accretion phase has ended.

At first sight, the difference in the onset time for HII regions from different models implies that the relative incidence of the smallest and earliest HII regions may allow different models to be discriminated. However, subsequent differences in the expansion rate of the HII regions may be complicated matters. For example, the rapid expansion of HII regions into outflow cleared cavities (e.g. Tan & McKee 2003; Tanaka et al. 2016) in the McKee & Tan (2003) and Peters et al. (2010) should result in a dearth of small HII regions despite the early onset of the ionization. Neverthe-

less, it is clear that the main differences in these theoretical models arise at the earliest onset of the HII region phase and that studying the physical properties of youngest and smallest HII regions will help to improve our theoretical understanding of massive star formation.

Observationally, the smallest and densest HII regions so far discovered are commonly known as hyper-compact HII regions (HC HII) that have typical size $\lesssim 0.03\,\mathrm{pc}$, electron density $\gtrsim 10^6\,\mathrm{cm}^{-3}$, and emission measure $\gtrsim 10^{10}\,\mathrm{pc\,cm}^{-6}$ (Kurtz 2005). They are distinguished from the next largest class of HII regions, the ultra-compact HII regions (UC HII) that have typical size $\lesssim 0.1\,\mathrm{pc}$, electron density $\gtrsim 10^4\,\mathrm{cm}^{-3}$, and emission measure $\gtrsim 10^7\,\mathrm{pc\,cm}^{-6}$(Kurtz 2005), primarily because they show extremely broad radio recombination lines (RRL) (Hoare et al. 2007), with typical $\Delta V = 40-50\,\mathrm{km\,s}^{-1}$ and with some $\Delta V \gtrsim 100\,\mathrm{km\,s}^{-1}$ (Gaume et al. 1995; Johnson et al. 1998; Sewilo et al. 2004), compared to the typical $\Delta V = 25-30\,\mathrm{km\,s}^{-1}$ of UC HII regions (Wood & Churchwell 1989; Afflerbach et al. 1996). We summarize the observational properties of known HC HII regions from references in Table 1. As can be seen, the RRL line widths of HC HII regions, their emission measures (EM) and electron densities (n_e) are in general larger than those of UC HII regions, although there is considerable spread. The radio spectral indices of HC HII regions are positive with a typical value ~1 (Beuther et al. 2007), i.e., between the purely optically thick and optically thin values discussed by Kurtz (2005) which may, in turn, indicate line-of-sight density gradients (Keto 2003).

Another property of HC HII regions is their rarity, with only 16 confirmed HC HII regions in the references compared to ~600 UC HII regions (Urquhart et al. 2013; Lumsden et al. 2013; Cesaroni et al. 2015). However, it is not clear if this rarity is intrinsic or caused by observational biases. As most surveys for young HII regions have been carried out between 1.4 and 5 GHz, they unfortunately suffer from an observational bias towards the discovery of objects with flat or falling spectral indices. HC HII regions with strong positive spectra have 1.4–5 GHz fluxes orders of magnitude less than UC HII regions and are thus likely to have been missed in low-frequency surveys. The majority of the HC HII regions listed in Table 1 were discovered serendipitously by high-frequency observations of known UC HII regions.

Our current limited understanding of the number and global properties of HC HII regions mean that it is difficult to constrain theoretical models of massive star formation as these models predict differently at the very early evolution of HII regions. Secondly, it is also difficult to place HC HII regions into context with the more well-known UC HII regions. For example, the defining characteristics of size, electron density, and emission measure proposed by Kurtz (2005) fall on a continuous spectrum and so it is difficult to identify discrete "types". As we can see in Table 1 the sizes, emission measures, and electron densities of many of the identified "HC HII regions" fall within ranges that are more appropriate to UC HII regions. With only a handful of identified HC HII regions, it is difficult to identify a clear dividing line between the two types of HII regions. Understanding the evolution of the youngest and densest HII regions requires us to find more good examples.

We have undertaken the largest and most systematic search yet undertaken for HC HII regions. As Table 1 shows, the easiest defining observational characteristic of HC HII regions is their positive radio spectral index. While broad recombination line widths are a key observational feature of HC HII regions, routine spectroscopy of large numbers of faint Galactic radio sources will not be possible until the advent of the SKA (e.g. Thompson et al. 2015). We have used current radio interferometer surveys of the Galactic Plane, namely CORNISH (5 GHz, Hoare et al. 2012), MAGPIS (1.4 GHz, Helfand et al. 2006; White et al. 2005), and THOR (1~2 GHz, Bihr et al. 2016; Beuther et al. 2016), to identify objects with positive spectral indices. We then cross-match these positive spectrum radio sources with mid/far-infrared and submillimetre survey data to identify objects embedded within molecular clumps, as would be expected for the initial stages of massive star formation. This is a similar strategy that is used to identify source type in CORNISH [1]. Of course, the sample that we have assembled here is also subject to the observational bias towards negative and flat spectrum indices that we have previously mentioned. However by using this method we can nevertheless search for bright and HC HII regions and obtain a much wider understanding of young and dense HII regions.

This paper is organized as follows. Section 2 describes the Galactic Plane surveys we used to identify positive spectrum radio objects and confirm those that are embedded within molecular cloud clumps. The details of determining the spectral indices and identifying a sample of objects with rising radio spectra is presented in Section 3. In Section 4, we characterize the properties of the sample at far-infrared (FIR) and submillimeter (submm) wavelengths, select a subsample of young and compact HII regions and discuss their properties. In particular, we compare the properties of HII regions with rising (positive) radio spectra to those with flat or negative spectra and dwell upon the implications of our survey for the frequency of HC HII regions in the Galaxy. In Section 5 we present a summary of our conclusions.

2 GALACTIC PLANE SURVEYS IN THE RADIO, FIR, AND SUBMM

In this section, we describe the individual Galactic Plane surveys that we have used to firstly identify a sample of positive spectrum radio sources, and secondly determine that these sources are indeed embedded HII regions.

Our starting point in the procedure was the CORNISH (Coordinated Radio "N" Infrared Survey for High-mass star formation), which we used to form a base 5 GHz radio source catalog. CORNISH is a sensitive ($\sim 0.4\,\mathrm{mJy\,beam}^{-1}$) and high-resolution ($\sim 1.5''$) of the survey region ($10^\circ < \ell < 65^\circ$ and $|b| < 1^\circ$) , using the JVLA in B and BnA configuration at 5 GHz, and has detected 3062 continuum sources greater than 7σ (Hoare et al. 2012; Purcell et al. 2013). Building upon CORNISH we used three other 1.4 GHz radio surveys to determine 1.4–5 GHz spectral indices (or lower limits to spectral index where only 1.4 GHz upper limits were available), MAGPIS, THOR and the White et al. (2005) VLA Galactic Plane survey.

The Multi-Array Galactic Plane Imaging Survey [2] has

[1] http://cornish.leeds.ac.uk/public/cone.php
[2] http://third.ucllnl.org/gps/index.html

Table 1. Summary of HC HII regions: Name and Galactic name, radio recombination lines (RRL) and its line width (FWHM), spectral indices, heliocentric distance (Dist.), linear diameter (Diam.), electric density (n_e), emission measure (EM), and reference.

Name	Gname	RRL (FWHM) Hnα (km s^{-1})	Spectral Index	Dist. (kpc)	Diam. (pc)	n_e (10^5 cm^{-3})	EM (10^8 pc cm^{-6})	Reference
Sgr B2 F	G000.6667−00.0362	H66α (80)	0.95 (1.4-22.5GHz)	8.5	0.011	~ 10	~ 10	3,6
G10.96+0.01 W	G010.9583+00.0223	H92α (43.8)	~1.2 (1.4-5GHz)	14	0.121	0.29	0.53	6,10
M17-UC1	G015.0346−00.6771	H66α (47)	1.1 (1.5-22GHz)	2.2	0.006	3.3	2.6	5,6
G24.78+0.08A1	G024.7898+00.0833	H66α (40)	-	7.7	0.002	–	–	8
G28.2−0.04 N	G028.2002−00.0495	H92α (74)	1.0±0.1 (1.4-15GHz)	5.7	0.028	0.76	1.9	6,10,12
G34.26+0.15 B	G034.2580+00.1533	H76α (48.4)	0.9 ± 0.4(5-23GHz)	3.3	0.008	2.2	4.3	6,7
G35.58−0.03	G035.5780−00.0313	H30α (43.2)	0.32±0.04 (8.3-23GHz)	10.2	0.018	3.3	19	9
W49 AA	G043.1653+00.0128	H66α (53.7)	0.6 (8.3-43GHz)	11.4	0.035	0.55	2.2	4,6
W49 AB	G043.1660+00.0120	H66α (63.9)	~1.1(8.3-43GHz)	11.4	0.031	0.45	1.3	4,6
W49 AG	G043.1666+00.0110	H66α (48.6)	~2 (22-43GHz)	11.4	0.061	0.33	1.4	4,6
G45.07+0.13 NE	G045.0712+00.1322	H76α (40)	–	6.0	0.032	0.94	1.9	10,12
W51e2[a]	G049.4898−00.3874	H66α (54)	–	7.0	0.02	16	–	12,13
NGC 7538-IRS1	G111.5382+00.8112	H66α (180)	~0.9 (23-50GHz)	3.5	0.04	1.2	2.1	1,6,12
G301.1366−00.2248	G301.1366−00.2248	H70α (66)	1.5 (0.843-20GHz)	4.5	0.02	6.8	30	11
G309.9217+00.4788	G309.9217+00.4788	H70α (40)	1.2 (0.843-20GHz)	5.5	0.03	2.3	8	11
G323.4594−00.0788	G323.4594−00.0788	H70α (50)	0.8 (0.843-20GHz)	4.8 / 8.9	0.05	0.64	1.9	11

Reference: 1, Gaume et al. (1995); 2, Shepherd et al. (1995); 3, de Pree et al. (1996); 4, De Pree et al. (1997, 2004); 5, Johnson et al. (1998); 6, Sewilo et al. (2004). 7, Avalos et al. (2006); 8, Beltrán et al. (2007); 9, Zhang et al. (2014); 10, Sewiło et al. (2011); 11, Murphy et al. (2010); 12, Keto et al. (2008); 13, Shi et al. (2010).

Table 2. Information of Galactic Plane surveys: survey name, wavelength and beam size, 1σ sensitivity, longitude (ℓ) and latitude (b) coverage, and reference.

Survey	Wavelengths &Beam	Sensitivity (mJy beam^{-1})	ℓ coverage °	b coverage °	Reference
CORNISH	5 GHz & 1.5″	0.4 (1σ)	10< l < 65°	| b | < 1°	1
MAGPIS	20 cm & 6″	~0.3 (1σ)	10<l<32°	| b | < 0.8°	2
THOR	1–2 GHz & 10–25″	0.3–1 (1σ)	14.0<l<37.9°& 47.1< l <51.2°	| b | ≤ 1°	3
White2005	20 cm & 6″	~0.9 (1σ)	10< l < 39° 39≤ l < 65°	| b | < 1° | b | < 0.8°	4
Total overlapping sky region		l = 10–39°,47.1–51.2° l = 39.0–65°	& &	| b | < 1° | b | < 0.8°	
Hi-GAL	250 μm & 18″	~ 12.8 (1σ)	| l | ≤ 60°	| b | ≤ 1°	5
ATLASGAL	870 μm & 19″	~50–70 (1σ)	-60< l < 60°	| b | < 1.5°	6

Reference: 1, Hoare et al. (2012); Purcell et al. (2013); 2, Helfand et al. (2006); 3, Bihr et al. (2016); Beuther et al. (2016); 4, White et al. (2005); 5, Molinari et al. (2010); 6, Schuller et al. (2009).

Table 3. Process of the cross-matching

Selection process of 1.4 GHz counterparts with $\alpha - d\alpha > 0$				
Overlapping CORNISH	Match selection	Unique matched sources	Positive spectrum objects	unresolved (resolved)
THOR	matching radius = 20″	remove duplicates	$\alpha - d\alpha > 0.0$	$S_{int} \leq 1.2S_{peak}$ ($S_{int} > 1.2S_{peak}$)
l = 14.0–37.9°, | b | < 1° l = 47.1–51.2°, | b | < 1°	1060 →	556 →	108 →	106 (2)
MAPGIS	matching radius = 6″	remove duplicates	$\alpha - d\alpha > 0.0$	$S_{int} \leq 1.2S_{peak}$ ($S_{int} > 1.2S_{peak}$)
l = 10–32°, | b | < 0.8°	647 →	647 →	126 →	58 (68)
l = 32–48.5°, | b | < 0.8°	53 →	53 →	25 →	24 (1)
White2005	matching radius = 6″	remove duplicates	$\alpha - d\alpha > 0.0$	$S_{int} \leq 1.2S_{peak}$ ($S_{int} > 1.2S_{peak}$)
10< l < 39°, | b | < 1° 39≤ l < 65°, | b | < 0.8°	963 →	397 →	151 →	68 (83)
In total	2723 →	1653 →	410 →	256 (154)
Selection process of 1.4 GHz dropouts with $\alpha_{min} > 0$				
Overlapping CORNISH	Unmatched selection	Exclude extended source	Unique sources	Positive spectrum objects
THOR	Removing those within 30″	$d_{sep} > 1.2d_{\text{THOR source}}$	remove duplicates	$\alpha_{min} > 0.0$
l = 14.0–37.9°, | b | < 1° l = 47.1–51.2°, | b | < 1°	173 →	123 →	118 →	87
MAPGIS	Removing those within 10″	$d_{sep} > 1.2d_{\text{MAGPIS source}}$	remove duplicates	$\alpha_{min} > 0.0$
l = 10–32°, | b | < 0.8°	102 →	101 →	6 →	6
White2005	Removing those within 10″	$d_{sep} > 1.2d_{\text{White2005 source}}$	remove duplicates	$\alpha_{min} > 0.0$
10< l < 39°, | b | < 1°	755 →	716 →	11 →	5
39≤ l < 65°, | b | < 0.8°	566 →	523 →	53 →	26
In total	1569 →	1463 →	188 →	124

Detailed description of selecting process are shown in the section 3.1 and section 3.2. a, Only a catalog within l = 5–32°, \| b \| < 0.8° has been published from MAGPIS (Helfand et al. 2006). We also take advantage of the image cutouts at l = 32–48.5° and \| b \| < 0.8° from MAPGIS website [2] to check the result by using AEGEAN package (Hancock et al. 2012). b, Only a catalog within l = 14.0–37.9°, l = 47.1–51.2°, \| b \| ≤ 1° has been published from THOR (Bihr et al. 2016). c, Only the overlapping region with CORNISH is presented, and the total sky region of White et al. (2005) is l = -20–120° and b = ± 0.8–±2.7°.

the highest sensitivity and resolution of the 1.4 GHz surveys that we have used, with a resolution of ∼ 6″ and noise level ∼ 0.3 mJy beam^{-1} (MAGPIS, Helfand et al. 2006) and a catalog has been published in the survey region 5< ℓ < 32°and | b | < 0.8°. MAGPIS images are also available between l = 32–48.5°and | b | < 0.8°, but no catalog of objects detected within these images has yet been published. We used image cutouts available from the MAPGIS website [2] to examine the 1.4 GHz counterparts to CORNISH sources in the uncatalogued region of the Galactic Plane. For further details see Section 3.2.

To cover the remainder of the CORNISH survey region, we use catalogs and data from the HI, OH, Recombination line survey of the Milky Way (THOR, Bihr et al. 2016; Beuther et al. 2016) at 1–2 GHz and the 20 cm VLA survey White et al. (2005), hereafter White2005. Details of all four surveys are given in Table 2. The complete region covered by these radio surveys is ℓ = 10–39°& ℓ = 47.1–51.2°and | b | < 1°, ℓ = 39.0–65°and | b | < 0.8°.

Once the 1.4–5 GHz radio spectral index of the objects has been derived, we select those objects with a positive spectral index and then confirm that they are embedded within molecular cloud clumps. We inspect the morphology of each positive spectrum source in the ATLASGAL and Hi-GAL surveys. The APEX Telescope Large Area Survey of the Galaxy (ATLASGAL), has a resolution of 19″ and typical noise level of 50 to 70 mJy beam^{-1} (Schuller et al. 2009), providing the largest, unbiased database for detailed studies of large numbers of early stages of massive-star forming clumps in the Galaxy. The Herschel infrared Galactic Plane Survey (Hi–GAL) aims to detect the earliest phases of the formation of molecular clouds and high-mass stars at five bands (Molinari et al. 2010, 2016). We used the most sensitive band of Hi-GAL at the 250 μm, which has a resolution of 18″ that is similar to ATLASGAL beam of 19″ and has a 1σ flux density sensitivity of 12.8 mJy beam^{-1}. The 250μm band lies close to the peak of the SED of cold dust and is thus an excellent tracer of molecular clumps.

3 DETERMINING THE RADIO SPECTRAL INDEX

The spectral index of a radio source is defined by a power law relationship between its flux density S_ν and frequency ν ($S_\nu \propto \nu^{+\alpha}$) [3]. In practice the spectral index is determined between two flux densities S_{ν_1} and S_{ν_2} measured at two specific frequencies ν_1 and ν_2 using the following equation

$$\alpha = \frac{\log(S_{\nu_2}/S_{\nu_1})}{\log(\nu_2/\nu_1)} \quad (1)$$

The true value of the spectral index α can only be determined when both fluxes in Equation 1 are available. Nevertheless, it is possible to determine a lower limit to the spectral index $\alpha_{\rm min}$ for sources that are only detected at a higher frequency (5 GHz in our case) but not at the lower (1.4 GHz) by using an upper limit for the flux density at the lower frequency, i.e.

$$\alpha_{\rm min} = \frac{\log[(S_{5GHz} - dS_{5GHz})/(5 * dS_{1.4GHz})]}{\log(5/1.4)} \quad (2)$$

where dS_ν represents the 1σ r.m.s. error in the flux density at frequency ν. Note that this equation assumes a 5σ detection threshold to determine the upper limit and also subtracts the 1σ error from the 5 GHz measurement to determine a reliable lower limit to the spectral index. In the following subsections, we present our method of determining α and $\alpha_{\rm min}$ from the CORNISH, MAGPIS, THOR and White2005 surveys. The individual steps in the process are summarized in Table 3.

3.1 CORNISH sources with 1.4 GHz counterparts

Using the CORNISH and MAGPIS/White2005/THOR source catalogs, we select CORNISH catalog sources that are positionally associated with corresponding MAGPIS/White2005/THOR catalog sources. As the MAGPIS and White2005 1.4 GHz surveys have resolutions of 6″, we use a circular matching threshold of 6″. Because the angular resolution of THOR is 10–25″, we choose the same matching threshold of 20″ used in THOR (Bihr et al. 2016), to identify sources which are detected in both CORNISH and THOR. Using these matching criteria we obtain 700, 963, and 1060 matches to CORNISH sources from MAGPIS, White2005, and THOR respectively.

Next, we remove duplicates caused by overlapping survey regions and create a unique list of matching sources by merging the MAGPIS, White2005 and THOR matches. Duplicates are removed by choosing the counterpart from the survey with the highest sensitivity at the CORNISH source position. In general, MAGPIS has the highest sensitivity, followed by THOR and finally by White2005. In this search, we must also take into account the fact that a MAGPIS catalog has not been published for the region between ℓ = 32–48.5°. So, for all CORNISH sources lying in this region of the Plane, we inspected MAGPIS cutout images obtained from the MAGPIS website and for those with 1.4 GHz counterparts, measured their peak and integrated fluxes using the AEGEAN package (Hancock et al. 2012). 53 CORNISH sources in this region were found to have MAGPIS counterparts. Overall, the matching process resulted in 700 MAGPIS matches, 556 THOR matches, and 397 White2005 matches respectively.

Finally, as we are principally interested in positive spectrum sources in this study, we calculate the 1.4–5 GHz spectral index of each source using Equation 1 and remove all sources whose spectral index α is less than zero. This process gives a final positive spectrum ($\alpha - {\rm d}_\alpha > 0$) catalog of 410 sources; 108 from THOR matches, 151 from MAGPIS matches, and 151 from White2005 matches.

As this sample includes both point sources and extended sources, we need to bear in mind that the radio surveys are interferometric and carried out at different frequencies and with different VLA configurations. Thus, each survey has different a coverage of the uv plane, and so we are only able to derive reliable spectral indices for point sources. We use the same criterion to distinguish between point and extended sources as the THOR survey (Bihr et al. 2016), where extended sources are identified as those having an integrated

[3] note that in some, mainly extragalactic, studies Equation (1) is defined as $S \propto \nu^{-\alpha}$.

1.4 GHz flux density more than 1.2 times their peak 1.4 GHz flux density ($S_{int}/S_{peak} > 1.2$). Because lower frequency surveys are more sensitive to extended emission than higher frequency survey, the flux densities of extended objects at 1.4 GHz surveys would contain more extended emission than 5 GHz CORNISH. One way to address this would be to combine multiple VLA configurations with single-dish data to improve the *uv* coverage and include zero-spacing flux (e.g. Tian & Leahy 2005, 2006). However, this is not feasible for the survey data that we use here.

Theoretically, the extremely small physical size of HC HII regions ($\lesssim 0.03$ pc) makes them highly likely to be point sources even in these interferometric radio surveys. However, most HC HII regions are located in complex star formation regions and/or surrounded by more diffuse ionized gas (Sewilo et al. 2004; Sewiło et al. 2011), which tends to result in more extended emission, particularly at lower frequencies which are more sensitive to extended low-density emission. Thus, the 1.4 GHz flux density of HC HII regions may be contaminated by their environment and exhibit more extended emission than at 5 GHz. We give two examples of this in Figure 1 and 2, which show the morphology of two known HC HII regions at 1.4 GHz (white contours) and 5 GHz (lime contours). The lower frequency emission traced by MAGPIS is clearly extended in both sources — by a neighbouring UC HII region in HC HII G45.07+0.13 NE (Figure 1) and by an extended emission in HC HII W49A G (Figure 2) whose integrated emission $S_{int} = 1.5\,S_{peak}$.

Therefore, we consider that the spectral indices of extended sources in the sample should be strictly considered as lower limits, and we have identified them as such in our results. In total, we obtain 256 point sources with reliable spectral indices and 154 sources that are extended at 1.4 GHz with lower limits to their spectral index.

3.2 1.4 GHz dropouts in CORNISH: spectral index lower limits

As well as deriving the spectral index from measurements at both 1.4 and 5 GHz, it is also possible to determine a lower limit to the spectral index as described in Equation 2. In order to derive $\alpha_{\rm min}$ we need to identify sources in the CORNISH catalog that do not possess counterparts in any of the 1.4 GHz surveys (aka 1.4 GHz "dropouts"). We do this by searching for sources in the CORNISH catalog that do not lie within 30″of *any* source within the THOR catalog and 10″ of *any* source within the MAGPIS and White 2005 catalogs (the differing search radii result from the differing beam sizes of the three 1.4 GHz surveys). That is to say, for each CORNISH source, we search for a THOR source inside a circle of 30″ radius and a MAGPIS/White2005 source within 10″ radius. If no 1.4 GHz sources lie inside this circle, the CORNISH source is preliminarily believed to be only detected at 5 GHz by CORNISH. An initial list of 173, 102, and 1323 dropout sources is obtained from THOR, MAGPIS, and White2005 respectively by this step.

As a secondary constraint, to avoid associations with large, extended THOR/MAGPIS/White2005 sources (which may contain sources extending over several arc minutes) we also require each CORNISH source found in the first step to have a separation from each THOR/MAGPIS/White2005 source greater than 1.2 times the THOR/MAGPIS/White2005 source angular diameter. With this step, we remove the very large angular diameter THOR/MAGPIS/White2005 sources that may appear as "over-resolved" by CORNISH which is not as sensitive to large-scale structure. This constraint reduces the samples to 123, 101, and 1245 sources for THOR, MAGPIS, and White2005 respectively.

Next, we create a unique catalog by merging the individual THOR, MAGPIS and White2005 dropouts and removing the duplicates caused by the overlapping survey regions. Where measurements were taken of a CORNISH source by more than one of THOR, MAGPIS or White2005, we remove the measurements with the highest noise values and keep the most sensitive measurement (generally this belongs to the THOR or MAGPIS surveys). Again we must also take into account the fact that only a portion of the MAGPIS images have had catalogs published: the region between $\ell = 10{-}32°$is cataloged in Helfand et al. (2006), whereas only reduced images are presented on the MAGPIS website[2] for the region between $\ell = 32{-}48.5°$. So for each qualifying CORNISH source located between $\ell = 32{-}48.5°$, we inspected corresponding cutouts of the MAGPIS data[2], to determine if there is a 1.4 GHz counterpart detected by MAGPIS. if there is no 1.4 GHz counterpart in MAGPIS then the RMS noise of MAGPIS was measured at the position of the CORNISH source. Overall we found a total of 188 CORNISH sources that do not have 1.4 GHz counterparts in the THOR, MAGPIS or White2005 surveys (118 THOR dropouts, 6 MAGPIS dropouts, and 64 White2005 dropouts).

Finally, we calculated a lower limit to the spectral index ($\alpha_{\rm min}$) for each source using the CORNISH flux density and a 5σ upper limit to the 1.4 GHz flux at the CORNISH position obtained from the noise maps of the THOR, MAGPIS, and White2005 surveys. Again as we are principally interested in positive spectrum sources, we filter out those sources with $\alpha_{\rm min} < 0$ and list the remaining 124 positive spectrum objects in Appendix Table A2.

3.3 Selection of HII regions from the sample

Using the methods outlined in the previous section, we have identified a total of 256 radio sources whose spectral index $\alpha - \mathrm{d}_\alpha > 0$ and a further 278 positive spectrum objects with a minimum spectral index $\alpha_{\rm min} > 0$, obtaining a initial sample of 534 positive spectrum objects. We present this sample in Appendix Table A2. However, radio sources with positive spectra are not just limited to HC HII regions, and this sample is likely comprised of radio galaxies, planetary nebulae, and HII regions. Moreover, we must also bear in mind that the radio surveys used here were not observed simultaneously and so intrinsically variable sources may result in the derivation of incorrect spectral indices. In order to select HII regions from our sample of positive spectrum objects, we use the Hi-GAL and ATLASGAL surveys to identify those radio sources that are also associated with far-infrared and sub-mm emission. Our approach mirrors two recent studies to identify young and ultracompact HII regions (Cesaroni et al. 2015; Urquhart et al. 2013).

We inspected the appearance of each positive spectrum radio source in ATLASGAL 870 μm and Hi-GAL 250 μm cutout images and identified those radio sources that are positionally associated with compact 870 and 250 μm emission.

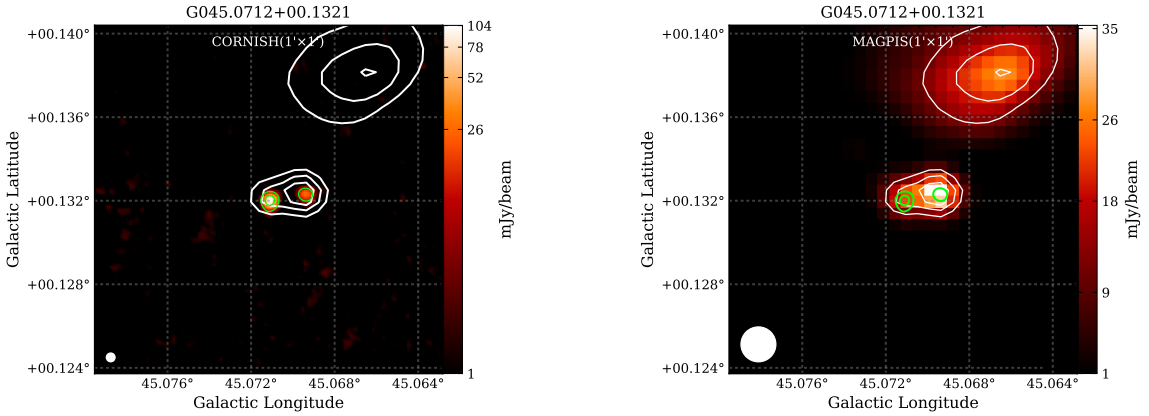

Figure 1. Left: the image of known HC HII G45.07+0.13 NE (CORNISH counterpart: G045.0712+00.1321) at 5 GHz CORNISH. Right: the image of known HC HII G45.07+0.13 NE at 1.4 GHz MAGPIS. The beams of CORNISH (1.5″) and MAGPIS (6″) are white circles presented in the lower left corner of each image. Overlaid lime and white contours on each image show 5 GHz emission from CORNISH and 1.4 GHz emission from MAGPIS, respectively. This is a example of HC HII region with nearby UC HII region show extended emission at 1.4 GHz (S_{int}/S_{peak} = 1.74) and we regard its spectral index as a lower limit (α_{min}).

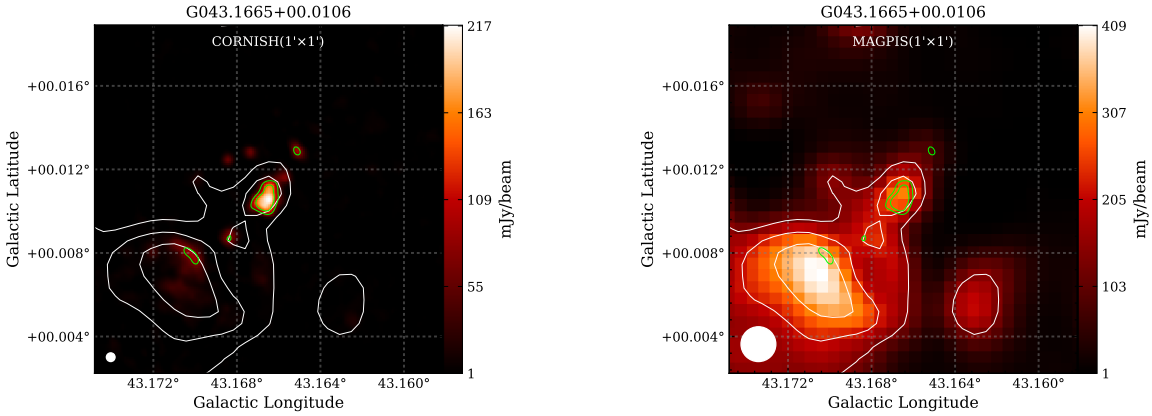

Figure 2. Left: the image of known HC HII W49A G (CORNISH counterpart: G043.1665+00.0106) at 5 GHz CORNISH. Right: the image of known HC HII G43.1665+00.0106 at 1.4 GHz MAGPIS. The beams of CORNISH (1.5″) and MAGPIS (6″) are white circles presented in the lower left corner of each image. Overlaid lime and white contours on each image show 5 GHz emission from CORNISH and 1.4 GHz emission from MAGPIS, respectively. This is a example of separate HC HII region show extended emission (S_{int}/S_{peak} = 1.5) at 1.4 GHz MAGPIS in our sample and we regard its spectral index as a lower limit (α_{min}).

These radio sources are likely to be located within molecular cloud clumps, and so represent young HII regions still in their embedded phase. We show two examples of known HC HII regions and their far-infrared and sub-mm morphologies in Figure 3 to illustrate their association with compact FIR and sub-mm emission. It is possible that a small number of these sources are chance alignments of background radio galaxies with foreground ATLASGAL and/or Hi-GAL sources. However we expect the number of these alignments to be small, as the total number of chance alignments for CORNISH was estimated by Urquhart et al. (2013) to be 14±4, and the majority of radio galaxies exhibit a negative spectral index. Hence, the number of chance alignments in our sample is expected to be statistically insignificant.

Of the 534 objects in our positive spectrum sample, 26 sources lie outside of ATLASGAL and Hi-GAL surveys and so are excluded from further analysis. From the remaining 508 sources, we find that 120 of them are positionally associated with 870 μm and 250μm emission, and are thus highly likely to be young HII regions. We list this sample of 120 young positive spectrum HII regions in Appendix Table A1. We compare our sample of young positive spectrum HII regions to the young HII region and UC HII regions samples of Cesaroni et al. (2015) and Urquhart et al. (2013). Unsurprisingly, due to the similar selection process for embedded, we find an almost one-to-one match: out of 120 HII regions in our positive spectrum sample, 113 objects correspond to Cesaroni et al. (2015) young HII regions or Urquhart et al. (2013) UC HII regions. The only disparity between the numbers of objects in common arises because Cesaroni et al. (2015) merge individual radio sources in their study that are closer together than 11.5″ into a single artificial source. In summary, by combining ATLASGAL and Hi-GAL surveys with our positive spectrum radio source sample, we

have identified 120 embedded HII regions that show positive radio spectra.

3.4 Recovery of known HC HII regions

As a critical test of our method, we examine the recovery of the known HC HII regions presented in Table 1. Of these 16 known HC HII regions, 11 lie within the CORNISH survey region. With two exceptions, M17 – UC1 and W51e2[a], 9 HC HII regions are recovered by the CORNISH survey. However, when applying our method to identify positive spectrum radio sources, we find that 5 out of these 9 are not recovered.

The reason why we do not recover these sources is that they are all located within large complex regions with extended emission at 1.4 GHz, and their 1.4 GHz flux is seriously affected by the emission from their surroundings. Three HC HII regions (G34.26+0.15B, G24.78+0.08A1, G28.2–0.04 N) have strongly extended counterparts at 1.4 GHz which dominate their 5 GHz emission, resulting in an overall negative spectrum. Two HC HII regions (W49AA/AB) have no separate identified 1.4 GHz counterparts.

Our method is successful at recovering known HC HII regions that are not located in complex environments, and as such, complements the existing discovery space for these objects where all the known examples have been discovered within larger complexes of HII regions. Nevertheless, we must bear in mind that our search for potential HC HII regions is limited within complex regions and our sample almost certainly is a lower limit to the true number of HC HII regions in the Milky Way. Below we briefly discuss the known HC HII regions that were recovered by CORNISH and our search process.

3.4.0.1 G010.9584+00.0221: This source is the known HC HII region G10.96+0.01 W (i.e., G010.9583+00.0223 in Table 1) identified by Sewilo et al. (2004). In our study, G10.96+0.01 W has a derived spectral index of α_{min} = 1.1 which is consistent with $\alpha^{5}_{1.4}$ ~ 1.2 (Sewilo et al. 2004). It has angular size of 2.2″ at 5 GHz with a distance of 14 kpc(Sewilo et al. 2004), so its 5 GHz linear diameter is ~ 0.15 pc, which is slightly larger than 1.3 cm size ~ 0.121 pc from Sewiło et al. (2011) with synthesized beam 1.4″ × 0.8″. Its larger size and extended emission may result from surrounding diffuse ionized gas emission proposed by Sewilo et al. (2004) and Sewiło et al. (2011).

3.4.0.2 G035.5781–00.0305: Shown in Figure 3, right panel, it is closely associated with compact FIR and submm emission, and also shows emission at 1.1mm, MIR and NIR wavelengths from BGPS, GLIMPSE, and UKIDSS[1]. This source is resolved into two extremely close sources: western G35.578–0.030 and eastern G35.578–0.031 at JVLA 2 cm and 3.6 cm (Kurtz et al. 1994). The western one is the known HC HII region G35.58–0.03 discussed by Zhang et al. (2014). The low resolution observations at 5 GHz CORNISH and 1.4 GHZ MAGPIS recognized both of them as one source G035.5781–00.0305 due to the large-scale extended continuum emission. The presence of extended continuum emission comes from surrounding diffused ionize gas like other HC HII regions (e.g. Sewilo et al. 2004; Sewiło et al. 2011), which leads to a larger angular size of 2.5″ at 5 GHz with linear diameter ~ 0.1 pc. A derived spectral index of α_{min} = 1.3 between 1.4 GHz and 5 GHz is considered to be a lower limit as the extended continuum emission at 1.4 GHz (S_{int}/S_{peak} = 1.32).

3.4.0.3 G043.1665+00.0106: This is the HC HII region W49A G (G043.1666+00.0110) in the W49A complex (De Pree et al. 1997, 2004; Sewilo et al. 2004). With other two nearby HC HII regions W49A A and W49A B. All of these HII regions are detected by CORNISH, but only W49A G is recovered in MAGPIS and also White2005, with a derived spectral index of α_{min} = 1.4. Note that this spectral index should be strictly considered as a lower limit due to a moderately resolved 1.4 GHz MAGPIS counterpart (S_{int}/S_{peak} = 1.5), see Figure 2. The 1.4–5GHz spectral index that we derive is consistent with a previously determined value α ~ 2 between 22 GHz and 43 GHz (De Pree et al. 1997, 2004). We measure an angular size of 3.68″ at 5 GHz with a distance of 11.4 kpc, which corresponds to a 5 GHz linear diameter of ~ 0.2 pc. This size is larger than size determined at 3.6 centimeter (~ 0.061 pc at resolution of 0.8″ × 0.8″) from De Pree et al. (1997) as it shows extended emission from surrounding ionized gas at 5 GHz with resolution 1.5″.

3.4.0.4 G045.0712+00.1321: This source is the HC HII region G45.07+0.13 NE (G045.0712+00.1322) (Keto et al. 2008; Sewiło et al. 2011), which also has a nearby fainter UC HII region G045.0694+00.1323 (offset, ~ 6″) from CORNISH. Within MAGPIS these two objects are indistinguishable from each other. We derive a spectral index of α_{min} = 0.68, which should be considered to be a lower limit due to the source blending and possible extended nature at 1.4 GHz (S_{int}/S_{peak} = 1.74). We measure a angular size of 1.89″ at 5 GHz with a distance of 6 kpc, resulting in a 5 GHz linear diameter of ~ 0.05 pc, which is slightly larger than its size at 3.6 centimeter ~ 0.032 pc with synthesized beam 1.5″ × 1.4″) from Sewiło et al. (2011).

Overall, we find that all of the recovered HC HII regions display a larger angular size as measured in CORNISH compared to their discovery images at higher frequency (e.g. Sewilo et al. 2004; Sewiło et al. 2011). Moreover, each of the known HC HII region is not point source at 1.4 GHz, with a peak to integrated flux ratio greater than 1.2. This suggests that HC HII regions are surrounded by lower density ionized gas, implying that searches based on size alone may not recover new HC HII regions. This is analogous to the well-known extended emission that is found around UC HII regions (Kim & Koo 2001; Ellingsen et al. 2005), in which snapshot, limited *uv* coverage, observations of UC HII regions filtered out surrounding extended emission. Kim & Koo (2001) suggested that these HII regions were in fact comprised of a hierarchical structure where UC components remained largely embedded within cloud clumps but a much wider expansion of the HII region had occurred along the density gradient of the clump. This results in a hierarchy of scales for the ionized gas from ultracompact to extended. We may be seeing a similar phenomenon in our HC HII sample.

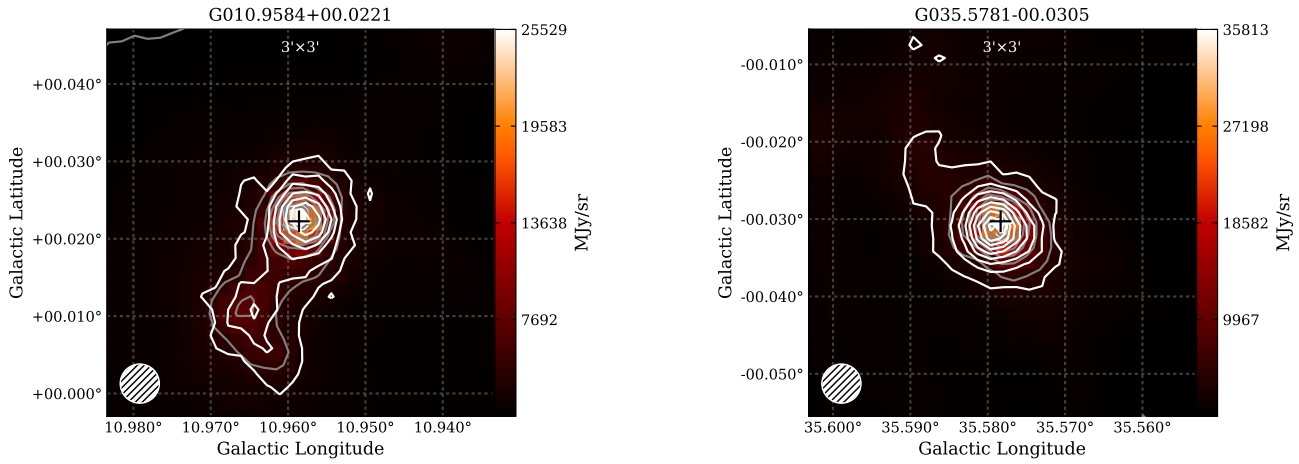

Figure 3. Left: the 250 μm image from Hi–GAL overlaid with 870 μm emission from ATLASGAL for HC HII region G10.96+0.01 W (CORNISH counterpart: G010.9584+00.0221). Right: the 250μm image from Hi–GAL overlaid with 870 μm emission from ATLASGAL for HC HII region G35.58−0.03 (CORNISH counterpart: G035.5781−00.0305). Grey and white contours on each image are determined by a dynamic range power-law fitting scheme (Thompson et al. 2006) show 250μm and 870μm emission respectively. The beam of Hi–GAL 250μm (18″) similar to ATLASGAL beam (19″) is shown in the lower left of each image. Cross indicates the position of the source at 5 GHz from CORNISH.

4 RESULTS & DISCUSSION

4.1 Observed Properties of the Sample

In this section, we examine the overall properties of the embedded positive spectrum HII regions that we have identified. We plot histograms of their spectral indices and linear diameters in Figure 4. Linear diameters have been derived using the 5 GHz angular diameters measured by CORNISH (Purcell et al. 2013) and the distances to the embedding molecular clumps determined by Cesaroni et al. (2015) and Urquhart et al. (2013).

We see that there are very few objects with purely optically thick spectral indices (i.e., $\alpha \sim 2$), even taking into account those with only strict lower limits. The maximum true spectral index in our sample is ∼1.5, and, when lower limits to the spectral index (α_{min}) are considered, the maximum value of α_{min} is ∼1.9. The mean values for $\alpha = 0.6 \pm 0.4$ and $\alpha_{min} = 0.5 \pm 0.4$. The majority of sources have spectral indices between 0 and 0.5. The linear diameters of the positive spectrum HII regions range between 0.02–1.2 pc, with a mean of 0.1±0.03 pc for objects with true values of α and 0.3±0.2 pc for objects with lower limits to their spectral index.

These two distributions are combined in Figure 5, where the spectral index is plotted against the linear diameter of the embedded positive spectrum HII regions. The canonical diameter for HC HII regions is shown by a horizontal dashed line at 0.03 pc. It is immediately obvious from Figure 5 that there are *no* positive spectrum HII regions that fulfil the Kurtz (2005) definition of diameter ≤ 0.03 pc and spectral index ∼ 2 (note that the exact Kurtz definition is based upon emission measure, but the proposed emission measure for HC HII regions of $\gtrsim 10^{10}$ pc cm^{-6} would result in $\alpha \simeq 2$, assuming a constant density structure which is almost certainly not the case). We do see objects with spectral indices greater than 1, but most of these have linear diameters ≥ 0.05 pc which is more consistent with the literature definition of the ultracompact HII region. The two small diameter sources ($d \leq 0.03$ pc) in our sample both have lower limits to their spectral index that are below one.

Interestingly, we also see larger ∼pc diameter HII regions that fit the definition of compact to classical HII regions, but with positive radio spectra rather than the −0.1 spectral index expected from optically thin emission. This suggests that these larger HII regions have density gradients indicating a mix of optically thin and thick components along the line of sight.

The lack of positive spectrum HII regions that fulfill the canonical picture for HC HII regions is puzzling. On the one hand, this may indicate that these regions are indeed rare. But on the other, we note that the known HC HII regions recovered in our search all show 5 GHz linear diameters larger than that expected for HC HII regions (the filled blue circles in Figure 5). Thus, the fact that we do not find any such regions fitting the expected definition may merely be the result of the definition being incorrect! If HC HII regions are indeed likely to be surrounded by lower density ionized gas in the same hierarchical structure, then their observed linear diameter will be a complex function of observing frequency and *uv* coverage. Thus, a number of the positive spectrum objects that we have identified may well be extremely young HC HII analogs with extended halos. Further high-resolution multi-frequency and multi-configuration observations are required to study morphology and physical properties of these objects over a range of size scales and determine whether our sample does indeed contain very young HII regions.

4.2 Comparison with Herschel and ATLASGAL selected HII regions

As mentioned in Section 3.3 we have compared our sample of positive spectrum HII regions to those presented in Ce-

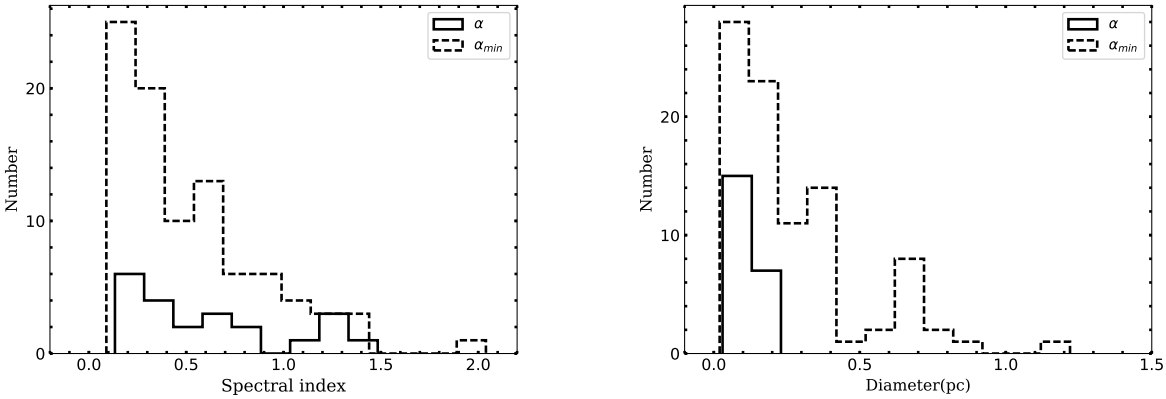

Figure 4. Left: the distribution of spectral indices of HII from our sample with average $\alpha = 0.6 \pm 0.4$ and average $\alpha_{min} = 0.5 \pm 0.4$. The bin size is 0.15 dex. Right: the distribution of angular diameter of this sample at 5GHz with average value of 0.1±0.03pc and 0.3±0.2 pc for α and α_{min} sample respectively. The bin size is 0.1.

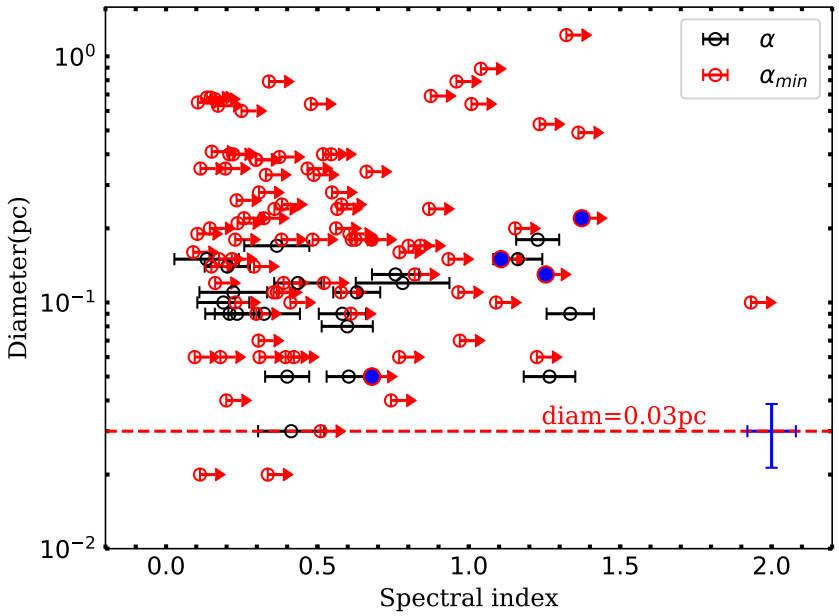

Figure 5. Spectral index (α) or the lower limit of spectral index (α_{min}) versus the linear diameter at 5 GHz of our sample. The filled blue circles show the four known HC HII regions recovered by this method. Characteristic errors for linear diameters show in blue in lower-right of the plot. Rightward pointing arrows represent a lower limit of the spectral index α_{min}. No obvious relation between spectral indices and linear diameter for α sample as well as α_{min} sample, however, it is not possible to obtain real trends for α_{min} sample.

saroni et al. (2015) and Urquhart et al. (2013). These samples were all selected similarly (i.e. by combining CORNISH, ATLASGAL and Hi-GAL) and this facilitates their cross-comparison. The added feature of our work is that we have determined the spectral index for our sample and so can split the Cesaroni et al. (2015) and Urquhart et al. (2013) samples by their spectral index to explore differences between populations. As both Cesaroni and Urquhart samples have well-determined physical properties (e.g. clump mass, luminosity, and Lyman continuum flux) we can examine trends in these quantities with spectral index.

We have combined the Cesaroni and Urquhart catalogs into one sample, eliminating duplicates between the two catalogs, and resulting in a final sample containing 251 young embedded HII regions drawn from CORNISH. We then cross-matched this against the CORNISH sources for which we determined a spectral index (or lower limit) in Section 3, and against the CORNISH sources associated with known HC HII in Table 1. This allows us to split the combined Cesaroni and Urquhart sample into two subsamples, those embedded HII regions with positive (or rising) spectra and those HII regions with flat or negative spectra (i.e., not-

rising spectra). We find 118 HII regions with rising spectra and 127 HII regions with not-rising spectra. The remaining 6 HII regions could not have their spectral indices determined and are excluded from further analysis.

Cesaroni et al. (2015) performed a similar although more limited analysis (see their Figure 1) using CORNISH and MAGPIS, in order to confirm the thermal nature of the emission from their HII region candidates. We find similar qualitative results to Cesaroni et al. (2015) in that roughly half of the sample show evidence for rising spectra with the remainder not-rising. The individual differences between our and the Cesaroni et al. (2015) results are due to the differing matching methods used (Cesaroni et al. (2015) use a simple 20″ matching radius and do not consider the confusing effect of large diameter sources in MAGPIS). We examine the differences in the physical properties between rising and not-rising spectrum subsamples in Figure 6 to Figure 8.

In Figure 6 (left-hand panel) we show the distribution of bolometric luminosity of the two subsamples. Although the means of the two subsamples are similar with a mean $\mathrm{Log(L/L_\odot)}$ of 4.4 ± 1.6 for rising spectrum HII regions compared to 3.6 ± 2.0 for not-rising HII regions, we do see a shift towards higher luminosities for rising spectra HII regions. A Kolmogorov–Smirnov (KS) test comparing the luminosity of the two subsamples yields a small p-value of 0.0011, and so we are able to reject the null hypothesis that the two subsamples are drawn from the same parent population.

We see a similar effect when we compare the Lyman continuum fluxes of rising and not-rising spectrum HII regions, shown in Figure 6 (right-hand panel). We take the values for Lyman continuum flux from Cesaroni et al. (2015) and Urquhart et al. (2013). Further details of the derivation can be found in these papers, but we note in passing that both studies assume optically thin emission at 5 GHz which may significantly underestimate the Lyman flux of optically thick emission. Comparing the means of the two subsample we find that the mean $\mathrm{N_{Ly}}$ for the rising spectrum HII regions ($\mathrm{Log(N_{Ly}(s^{-1}))} = 48.0 \pm 0.8$) is moderately larger than the not-rising spectrum HII regions ($\mathrm{Log(N_{Ly}(s^{-1}))} = 47.5 \pm 0.7$). A KS test of the Lyman fluxes of the two subsamples returns a p-value of 2×10^{-5}, and thus we are able to significantly reject the null hypothesis that the two subsamples are drawn from the same population. However, we must draw attention to the possibility of systematic bias in the rising spectrum sample due to optical depth effects. As this means that the Lyman fluxes for the rising spectrum HII regions may be underestimated, the true disparity between the subsamples may be greater than we have indicated. Kim et al. (2017) compared independent radio continuum and millimeter-wave recombination line analyses for a sample of HII regions, with the result that optical depth effects appeared not unduly to affect the results. However, further investigation of our rising spectrum sample is needed to confirm this hypothesis.

In Figure 7 and 8, we show the distributions of linear diameter, clump mass, and luminosity-to-mass ratio ($\mathrm{L/M(L_\odot/M_\odot)}$) for both rising spectrum and not-rising spectrum subsamples. All of these distributions are essentially indistinguishable for rising spectrum HII regions and not-rising spectrum HII regions. For linear diameter, the respective means for rising and not-rising subsamples are identical at 0.2 ± 0.2 pc and a KS test is unable to reject the null hypothesis with a p-value of 0.7. For clump mass we find respective means of $\log \mathrm{M_{clump}} = 3.5 \pm 0.6\,\mathrm{M_\odot}$ and $\log \mathrm{M_{clump}} = 3.4 \pm 0.7\,\mathrm{M_\odot}$ for rising and not-rising samples, and a KS test is again unable to reject the null hypothesis that the clump masses of each subsample are drawn from the same population. Finally, for the luminosity-to-mass ratio ($\mathrm{L_{bol}/M_{clump}}$) we find identical mean values for both subsamples ($\mathrm{mean \log L(L_\odot)/M(M_\odot} = 1.4 \pm 0.4$) and a KS test is unable to reject the null hypothesis that $\mathrm{L_{bol}/M_{clump}}$ values are drawn from the same population.

On balance, we find that the subsample of rising spectrum HII regions tend to have a higher bolometric luminosity and Lyman continuum fluxes but are not of significantly different linear diameter or found in clumps of different mass or luminosity-to-mass ratio than the not-rising spectrum HII regions. This suggests that rising spectrum HII regions may result from higher luminosity (and hence higher mass) stars with larger Lyman continuum fluxes. However, their similar linear diameters and luminosity-to-mass ratios imply an evolutionary status that may be much the same between the subsamples. The peak luminosities of $\sim 10^5 \mathrm{L_\odot}$ for the two subsamples HII regions (Figure 6) is consistent with the result in Davies et al. (2011, see their Figure 8) who discussed the relative number of HII regions as a function of luminosity based on data from both simulation and observation. In Figure 5, we see little evidence that the rising spectrum (i.e. potentially young, dense and optically thick) HII regions are consistent with the canonical HC HII description, which is observed by Urquhart et al. (2013).

We also investigate the millimeter-wave recombination line properties of our sample of positive spectrum HII regions by cross-matching against the aforementioned study of Kim et al. (2017). This sample of HII regions are selected from ATLASGAL clumps observed in millimeter-wave recombination lines, and we identify common objects in our two samples by matching common ATLASGAL clumps. In total, we find 35 HII regions in the positive spectrum sample that are associated with millimeter-wave recombination line detections from Kim et al. (2017). After filtering the example of one clump associated with two positive spectrum HII regions, we plot the recombination line widths against our derived spectral indices (α and α_{min}) in the right-hand panel Figure 8.

Figure 8 shows a generally positive trend between the recombination line width and spectral index, in that HII regions with broader line widths have larger spectral indices. However, it is difficult to confirm this as a genuine relationship between line width and spectral index as many of the spectral indices plotted here are strict lower limits rather than true values. We also indicate in Figure 8 the commonly-chosen dividing line between HC HII regions and UC HII regions at a line width of $40\,\mathrm{km\,s^{-1}}$. While objects with line widths in excess of 40 $\mathrm{km\,s^{-1}}$ do display larger spectral indices, there is no clear distinction between the two.

4.3 Implications for the frequency of HC HII regions and the formation of massive stars

The over-riding feature of our results is that HC HII regions following the canonical definition of Kurtz (2005) are not common in our sample. This was also noted by Kim et al. (2017) who found no hypercompact or high emission mea-

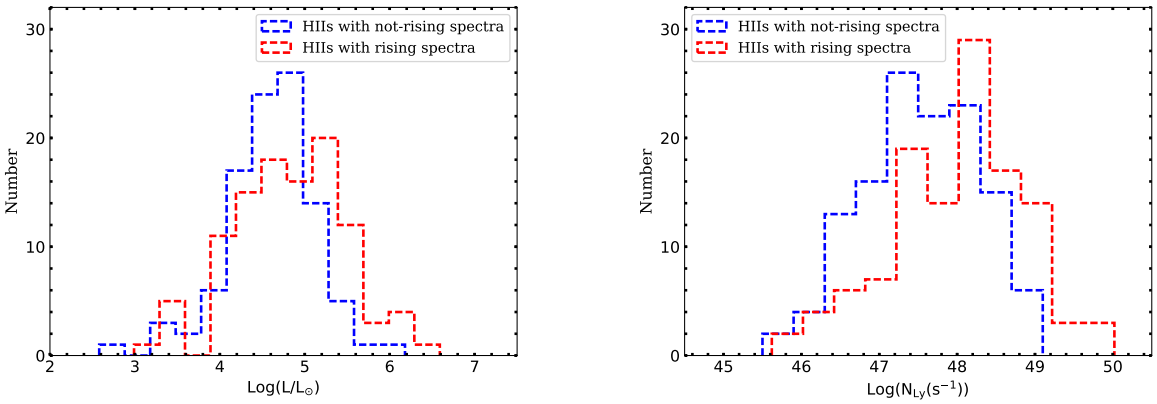

Figure 6. Left-hand panel: the distribution of bolometric luminosity for rising spectra young HII region and not-rising spectra young HII regions, with mean value of Log(L/L$_\odot$) = 4.4 ± 1.5 and Log(L/L$_\odot$) = 3.6 ± 2.0, respectively. The bin size is 0.3. Right-hand panel: the distribution of Lyman continuum flux of UC HII regions with rising spectra and with not-rising spectra, with mean value of Log(N$_{Ly}$(s^{-1})) = 48.0 ± 0.8 and Log(N$_{Ly}$(s^{-1})) = 47.5 ± 0.7, respectively. The bin size is 0.4.

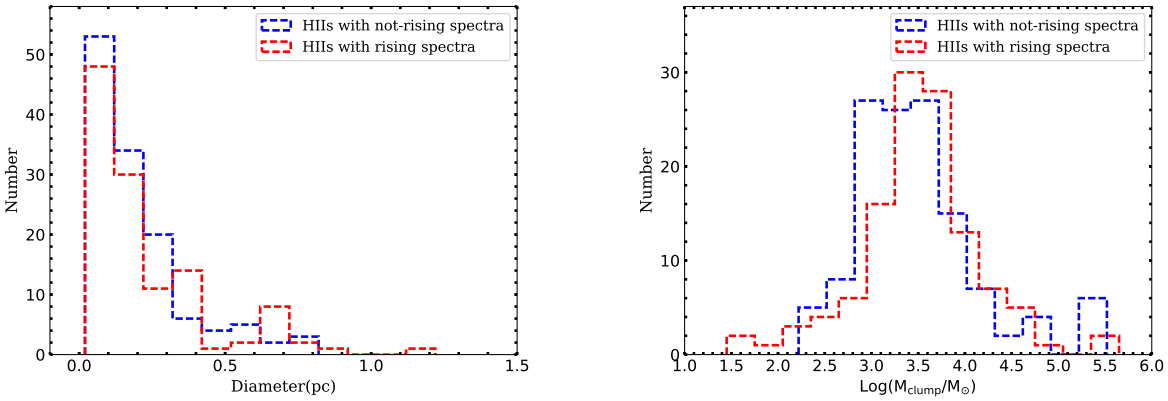

Figure 7. Left-hand panel: the distribution of linear diameter for rising spectra young HII region and not-rising spectra young HII regions, with the same mean value of diam = 0.2 ± 0.2 pc for the two sample. The bin size is 0.1. Right-hand panel: the distribution of clump mass of UC HII regions with rising spectra and with not-rising spectra, with mean value of Log(M$_{clump}$/M$_\odot$) = 3.5 ± 0.6 and Log(M$_{clump}$/M$_\odot$) = 3.4 ± 0.7, respectively. The bin size is 0.3.

sure HII regions in their 5 GHz selected sample. Kim et al. (2017) explain the lack of HC HII regions in their sample due to the observational bias that we discussed in Section 1. However, given that we have carried out a wide-area survey, demonstrated that CORNISH is able to recover approximately half of the known HC HII regions in Table 1 and that the recovered 5 GHz linear diameters of these objects are larger than the canonical definition of HC HII regions we do not feel that this is the most likely explanation. The true picture of HC HII regions is that they are likely to be comprised of a hierarchical structure similar to UC HII regions (e.g. Kim & Koo 2001), with highly compact dense, high emission measure "cores" surrounded by lower density, lower emission measure "halos". The distribution of spectral indices in our sample is indicative of this structure, with the majority of indices falling between 0 and 1 which implies mixed optically thin and thick emission along the line of sight. Thus the perhaps simplistic definition of HII regions based on size may, in fact, be complicated matters and should be revised to take account of the complex structure of these objects.

Nevertheless, in Figure 6, the rising spectrum HII regions (i.e., potentially young and dense) are more likely to be of higher luminosity and have higher Lyman continuum fluxes than the not-rising spectra HII regions. While Urquhart et al. (2013) found that the most highly luminous HII regions are amongst the largest. HII regions show an excess of Lyman continuum that the measured values are larger than the theoretical prediction, which cannot be easily explained (Lumsden et al. 2013; Urquhart et al. 2013). Thus, further research is needed to understand the slight difference of luminosity and Lyman continuum flux between the two subsamples HII regions.

It is difficult to assess how complete our observations are of the potential hypercompact population of HII regions. We find that CORNISH is able to recover roughly half of the

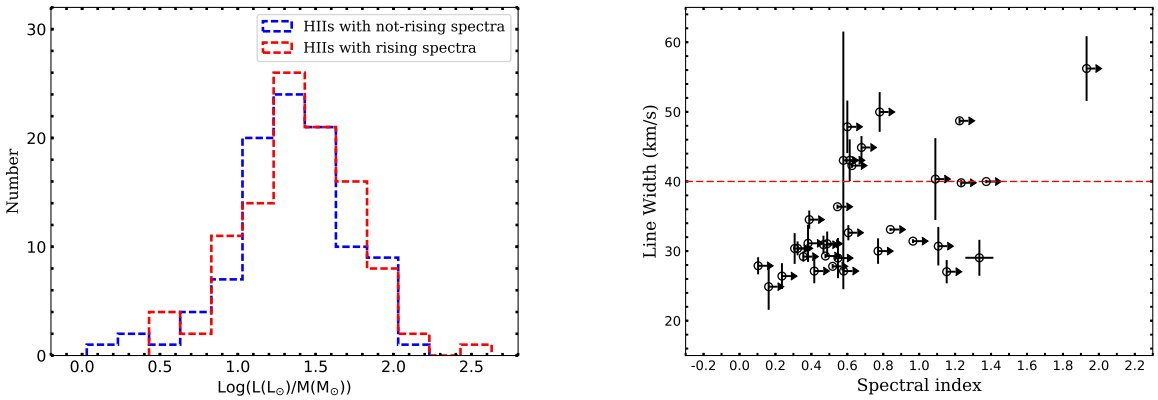

Figure 8. Left-hand panel: distribution of luminosity-to-mass ratio for rising spectra young HII region and not-rising spectra young HII regions, showing same mean value of $\mathrm{Log(L(L_\odot)/M(M_\odot))} = 1.4 \pm 0.4$ for both. The bin size is 0.2. Right-hand panel: spectral indices versus line widths of millimeter RRLs for 34 rising spectra HII regions. Rightward pointing arrows represent a lower limit of the spectral index α_{min}.

known sample of HC HII regions and so one might naively assume that there is perhaps a factor 2 more to be discovered in the CORNISH survey region. However, it is clear that HII regions with positive spectra are in fact common, as roughly half of the Cesaroni et al. (2015) and Urquhart et al. (2013) catalogs of compact and ultracompact HII regions have positive spectral indices. This may have implications as the ionized gas properties that have been derived in many studies of HII regions to date have assumed that the continuum emission is optically thin, rather than the mixture of optically thick and thin components that our distribution of spectral indices implies. Detailed multi-frequency and multi-configuration observations that can reveal the ionized structure of these regions on a range of scales are required to further investigate their nature and examine their relationship to the early phases of massive star formation.

5 SUMMARY AND CONCLUSIONS

We have carried out the largest and most unbiased search for hypercompact HII regions to date by combining radio surveys at 1.4 and 5 GHz (THOR, CORNISH, MAGPIS and White2005) with far-infrared and sub-mm Galactic Plane surveys (Hi-GAL and ATLASGAL). We obtain a sample of 534 objects with a 1.4 to 5 GHz spectral index greater than zero, listed in Appendix Table A2. 256 of these objects were detected at 5 GHz and as point sources at 1.4 GHz which means that we could determine true values of their spectral index, whereas the remaining 278 objects have upper limits at 1.4 GHz or were found to be moderately extended at 1.4 GHz and thus have strict lower limits to their spectral index. We identified HII regions in this sample using ATLASGAL and Hi-GAL surveys in a similar manner to the recent studies of young and ultracompact HII regions by Cesaroni et al. (2015) and Urquhart et al. (2013). We found a total of 120 HII regions with positive radio spectral indices, shown in Appendix Table A1. Among the 120 positive spectra HII regions, 35 have archival data of RRL, see the right-hand panel of Figure 8. Twelve out of the 35 HII regions show broad RRL line-width $\Delta V \gtrsim 40\,\mathrm{km\,s^{-1}}$, listed in Table 4. Four of the 12 sources are known HCHII regions in Table 1, and follow-up JVLA observations for the rest HII regions have been carried out to determine their nature. The physical properties of the 120 rising spectra HII regions were examined and compared to the Cesaroni et al. (2015), Urquhart et al. (2013) and Kim et al. (2017) samples of HII regions. We draw the following conclusions:

(i) We find *no* objects in our resulting positive spectrum HII region sample that match the canonical definition of HC HII regions given in Kurtz (2005), i.e. with linear diameter $\leq$ 0.03 pc and with a spectral index $\simeq 2$. The majority of our positive spectrum HII regions have diameters more than 0.03 pc and with spectral indices between 0.5–1.0.

(ii) We recover roughly half of the known HC HII regions in the CORNISH survey. However, these objects are generally resolved at 5 GHz with larger diameters than seen in their higher frequency discovery observations. Combined with spectral indices that indicate mixed optically thick and thin components along the line of sight, we suggest that HC HII regions have a hierarchical structure analogous to UC HII regions. Multi-frequency, multi-resolution radio observations are required to confirm this hypothesis. The canonical definition of HII regions based on linear diameter may perhaps need to be updated to reflect its structure.

(iii) We see a general trend between spectral index and the line width of mm-wave recombination lines observed by Kim et al. (2017), in that objects with higher spectral indices tend to show higher line widths. However, this trend is still inconclusive as many of the spectral indices for the Kim et al. (2017) sample are lower limits. Further higher frequency radio continuum observations are required to confirm this trend.

(iv) In a combined sample drawn from Cesaroni et al. (2015) and Urquhart et al. (2013) we find that roughly half of these HII regions have positive spectral indices. HII regions with a positive (i.e., rising) spectrum are found to be statistically more luminous and with higher Lyman fluxes than HII regions with negative or flat (i.e., not-rising) spectral indices. We find no evidence for differences in the linear diameter of

rising and not-rising spectrum HII regions, nor in the mass of their embedding clumps or their luminosity-to-mass ratios. This suggests that rising spectrum HII regions are associated with more luminous and massive stars.

ACKNOWLEDGEMENTS

We would like to thank the referee for the helpful comments. We acknowledge support from the NSFC (11603039, 11473038). H.B. acknowledges support from the European Research Council under the Horizon 2020 Framework Program via the ERC Consolidator Grant CSF-648505. M.A.T. acknowledges support from the UK Science & Technology Facilities Council via grant ST/M001008/1. A.Y. would like to thank the UK Science & Technology Facilities Council (STFC) and the China Scholarship Council (CSC) for grant funding through the China-UK SKA co-training programme.

APPENDIX A: TABLES

REFERENCES

Afflerbach A., Churchwell E., Acord J. M., Hofner P., Kurtz S., Depree C. G., 1996, ApJS, 106, 423
Avalos M., Lizano S., Rodríguez L. F., Franco-Hernández R., Moran J. M., 2006, ApJ, 641, 406
Beltrán M. T., Cesaroni R., Moscadelli L., Codella C., 2007, A&A, 471, L13
Beuther H. et al., 2016, A&A, 595, A32
Beuther H., Churchwell E. B., McKee C. F., Tan J. C., 2007, Protostars and Planets V, pp 165–180
Bihr S. et al., 2016, A&A, 588, A97
Cesaroni R. et al., 2015, A&A, 579, A71
Davies B., Hoare M. G., Lumsden S. L., Hosokawa T., Oudmaijer R. D., Urquhart J. S., Mottram J. C., Stead J., 2011, MNRAS, 416, 972
de Pree C. G., Gaume R. A., Goss W. M., Claussen M. J., 1996, ApJ, 464, 788
De Pree C. G., Mehringer D. M., Goss W. M., 1997, ApJ, 482, 307
De Pree C. G., Wilner D. J., Mercer A. J., Davis L. E., Goss W. M., Kurtz S., 2004, ApJ, 600, 286
Dyson J. E., Williams R. J. R., Redman M. P., 1995, MNRAS, 277, 700
Ellingsen S. P., Shabala S. S., Kurtz S. E., 2005, MNRAS, 357, 1003
Gaume R. A., Goss W. M., Dickel H. R., Wilson T. L., Johnston K. J., 1995, ApJ, 438, 776
Hancock P. J., Murphy T., Gaensler B. M., Hopkins A., Curran J. R., 2012, MNRAS, 422, 1812
Helfand D. J., Becker R. H., White R. L., Fallon A., Tuttle S., 2006, AJ, 131, 2525
Hoare M. G., Kurtz S. E., Lizano S., Keto E., Hofner P., 2007, Protostars and Planets V, pp 181–196
Hoare M. G. et al., 2012, PASP, 124, 939
Hosokawa T., Omukai K., 2009, ApJ, 691, 823
Hosokawa T., Yorke H. W., Omukai K., 2010, ApJ, 721, 478
Johnson C. O., De Pree C. G., Goss W. M., 1998, ApJ, 500, 302
Keto E., 2003, ApJ, 599, 1196
Keto E., Zhang Q., Kurtz S., 2008, ApJ, 672, 423
Kim K.-T., Koo B.-C., 2001, ApJ, 549, 979
Kim W.-J., Wyrowski F., Urquhart J. S., Menten K. M., Csengeri T., 2017, A&A, 602, A37
Kurtz S., 2005, in Cesaroni R., Felli M., Churchwell E., Walmsley M., eds, IAU Symposium Vol. 227, Massive Star Birth: A Crossroads of Astrophysics. pp 111–119
Kurtz S., Churchwell E., Wood D. O. S., 1994, ApJS, 91, 659
Lumsden S. L., Hoare M. G., Urquhart J. S., Oudmaijer R. D., Davies B., Mottram J. C., Cooper H. D. B., Moore T. J. T., 2013, ApJS, 208, 11
McKee C. F., Tan J. C., 2003, ApJ, 585, 850
Molinari S. et al., 2016, A&A, 591, A149
Molinari S. et al., 2010, PASP, 122, 314
Murphy T., Cohen M., Ekers R. D., Green A. J., Wark R. M., Moss V., 2010, MNRAS, 405, 1560
Peters T., Banerjee R., Klessen R. S., Mac Low M.-M., Galván-Madrid R., Keto E. R., 2010, ApJ, 711, 1017
Purcell C. R. et al., 2013, ApJS, 205, 1
Schuller F. et al., 2009, A&A, 504, 415
Sewilo M., Churchwell E., Kurtz S., Goss W. M., Hofner P., 2004, ApJ, 605, 285
Sewiło M., Churchwell E., Kurtz S., Goss W. M., Hofner P., 2011, ApJS, 194, 44
Shepherd D. S., Churchwell E., Goss W. M., 1995, ApJ, 448, 426
Shi H., Zhao J.-H., Han J. L., 2010, ApJ, 710, 843
Tan J. C., McKee C. F., 2003, ArXiv Astrophysics e-prints
Tanaka K. E. I., Tan J. C., Zhang Y., 2016, ApJ, 818, 52
Tenorio-Tagle G., 1979, A&A, 71, 59
Thompson M. et al., 2015, Advancing Astrophysics with the Square Kilometre Array (AASKA14), p. 126
Thompson M. A., Hatchell J., Walsh A. J., MacDonald G. H., Millar T. J., 2006, A&A, 453, 1003
Tian W. W., Leahy D., 2005, A&A, 436, 187
Tian W. W., Leahy D. A., 2006, A&A, 447, 205
Urquhart J. S. et al., 2013, MNRAS, 435, 400
White R. L., Becker R. H., Helfand D. J., 2005, AJ, 130, 586
Wood D. O. S., Churchwell E., 1989, ApJS, 69, 831
Zhang C.-P., Wang J.-J., Xu J.-L., Wyrowski F., Menten K. M., 2014, ApJ, 784, 107
Zinnecker H., Yorke H. W., 2007, ARA&A, 45, 481

This paper has been typeset from a TEX/LATEX file prepared by the author.

Table 4. 12 Rising Spectra HII regions with Broad Radio Recombination Lines (FWHM $\gtrsim 40\,\mathrm{km\,s^{-1}}$) in Our Sample

Gname CORNISH	$\mathrm{Flux}_{5\,GHz}$ (mJy)	Ang. (5 GHz) ($''$)	$\mathrm{Flux}_{1.4\,GHz}$ (mJy)	Spectral Index ($\alpha^5_{1.4}$)	Associated clump (AGAL)	ΔV(RRL) ($\mathrm{km\,s^{-1}}$)	Dist. (kpc)	Diam.(5 GHz) (pc)
G010.9584+00.0221†	195.97±18.33	2.20$''$	47.92±0.40	1.11*	AGAL010.957+00.022	43.8(H92α)	14	0.15
G030.5887-00.0428	92.37±8.33	1.79$''$	7.90±0.48	1.93*	AGAL030.588-00.042	56.2(H40α)	11.8	0.1
G030.7197-00.0829	969.33±96.01	4.59$''$	464.58±2.28	0.58*	AGAL030.718-00.082	43.0(H40α)	4.9	0.11
G030.8662+00.1143	325.47±32.96	3.09$''$	137.17±0.60	0.68*	AGAL030.866+00.114	44.9(H39α)	11.9	0.18
G033.1328-00.0923	378.59±34.75	4.02$''$	173.43±1.43	0.61*	AGAL033.133-00.092	43.0(H39α)	9.4	0.18
G034.2572+00.1535	1762.63±163.28	5.75$''$	370.78±3.39	1.22*	AGAL034.258+00.154	48.7(H42α)	2.1	0.06
G035.5781-00.0305†	187.75±18.44	2.53$''$	38.05±0.97	1.25*	AGAL035.579-00.031	50.0(H42α)	10.2	0.13
G043.1665+00.0106†	1365.68±125.16	3.68$''$	237.81±8.09	1.37*	AGAL043.166+00.011	40.0(H39α)	11.4	0.2
G045.0712+00.1321†	146.67±14.65	1.89$''$	61.6±0.6	0.68*	AGAL045.071+00.132	40.0(H76α)	6.0	0.05
G045.1223+00.1321	2984.27±274.33	7.46$''$	1345.96±1.67	0.63*	AGAL045.121+00.131	42.3(H41α)	4.4	0.16
G032.7441-00.0755	7.93±1.14	1.78$''$	0.34	1.09*	AGAL032.744-00.076	40.3(Hnα)	11.7	0.10
G045.4656+00.0452	62.26±5.79	1.70$''$	28.88±1.32	0.60±0.05	AGAL045.466+00.046	47.9(H39α)	6.0	0.05

These columns contain the Galactic name in CORNISH, flux density and angular scale (Ang.) of each source at 5 GHz, flux density at 1.4 GHz, and the spectral index and its error, and its ATLASGAL counterparts with Galactic name, line width of RRLs, heliocentric distance (Dist.) in kpc, and linear diameter (Diam.) at 5 GHz. Symbol † means the known HC HII regions recovered by this method. RRLs of Hnα (n = 39, 40, 41, 42) from Kim et al. (2017). References of H76α for HC HII G045.0712+00.1321 and H92α for HC HII G010.9584+00.0221 are same as Table 1. Symbol $\star$ means that sources with the lower limit of the spectral index. The flux density of G032.7441-00.0755 with no errors is the noise level at 1.4 GHz to the source position.

Table A1. Information of 120 young positive spectrum HII regions

Name Gal	ℓ (°)	b (°)	Flux$_{5GHz}$ (mJy)	Angular diameter ($''$)	Flux$_{1.4GHz}$ (mJy)	Spectral Index
G010.3009−00.1477†	10.30088	-0.1477	631.39±59.30	5.45±0.01	426.18±1.98	0.31
G010.4724+00.0275†	10.47236	0.0275	38.43±4.38	2.24±0.02	31.26±0.35	0.16
G010.6223−00.3788†	10.62231	-0.37877	483.33±49.87	5.76±0.01	327.63±1.89	0.31
G010.6234−00.3837†	10.6234	-0.38369	1952.22±176.18	4.64±0.00	571.28±1.88	0.97
G010.9584+00.0221†	10.95839	0.02206	195.97±18.33	2.20±0.00	47.92±0.40	1.11
G011.0328+00.0274†	11.03283	0.02738	5.69±1.06	1.89±0.15	3.71±0.28	0.34
G011.1104−00.3985†	11.11043	-0.39851	305.37±28.55	8.36±0.01	253.15±0.42	0.15
G011.1712−00.0662†	11.17121	-0.06621	102.17±12.73	10.75±0.04	83.15±0.32	0.16
G011.9368−00.6158†	11.93677	-0.61577	1155.90±105.38	5.89±0.00	735.63±0.43	0.36
G011.9446−00.0369†	11.94458	-0.03686	943.58±98.50	14.64±0.01	251.14±1.91	1.04
G012.1988−00.0345†	12.1988	-0.03447	62.71±5.92	2.68±0.06	47.56±0.31	0.22
G012.2081−00.1019†	12.20806	-0.10189	207.87±19.73	2.84±0.01	127.94±1.17	0.38
G012.4294−00.0479†	12.4294	-0.04791	45.17±4.35	2.72±0.07	24.39±1.26	0.48
G012.8050−00.2007†	12.805	-0.20067	12616.40±1120.83	16.23±0.01	4332.25±4.27	0.84
G012.8131−00.1976†	12.8131	-0.19759	1500.39±147.30	5.43±0.01	907.68±4.18	0.39
G012.9995−00.3583†	12.99951	-0.3583	20.14±3.70	3.09±0.32	10.52±0.28	0.51
G013.2099−00.1428†	13.20989	-0.14281	946.76±87.46	8.35±0.01	437.88±3.66	0.61
G013.3850+00.0684†	13.38496	0.06835	603.94±60.83	19.18±0.01	139.16±1.16	1.15
G014.7785−00.3328	14.77849	-0.33278	18.25±2.47	2.31±0.03	15.39±1.04	0.13±0.11
G016.1448+00.0088†	16.14482	0.00876	14.76±1.55	1.60±0.04	8.75±0.19	0.41
G016.3913−00.1383†	16.39128	-0.13827	124.27±15.43	11.74±0.04	40.83±0.31	0.87
G016.9445−00.0738†	16.94449	-0.07379	519.34±47.78	3.46±0.00	258.51±0.34	0.55
G017.0299−00.0696	17.02987	-0.06955	5.38±1.06	2.39±0.24	1.99±0.37	0.78±0.15
G017.1141−00.1124†	17.11407	-0.11236	17.21±2.19	2.83±0.16	14.22±0.25	0.15
G018.1460−00.2839†	18.14602	-0.2839	856.18±82.85	23.42±0.02	151.22±1.93	1.36
G018.3024−00.3910†	18.30241	-0.39103	1277.88±114.83	14.63±0.00	846.82±0.32	0.32
G018.4433−00.0056†	18.44328	-0.00558	81.31±7.30	2.41±0.04	56.18±0.37	0.29
G018.4614−00.0038†	18.46141	-0.00378	342.12±31.50	2.76±0.00	128.20±0.47	0.77
G018.6654+00.0294	18.66539	0.02935	5.65±0.85	1.74±0.10	3.74±0.21	0.32±0.12
G018.7106+00.0002	18.71061	0.00022	107.46±10.62	2.04±0.01	40.95±0.31	0.76±0.08
G018.7612+00.2630†	18.76118	0.26298	51.38±4.67	1.79±0.03	26.45±0.23	0.52
G018.8250−00.4675†	18.82499	-0.46749	11.41±2.17	2.53±0.25	9.08±0.35	0.18
G018.8338−00.3002†	18.83384	-0.30024	131.38±13.35	6.72±0.01	108.41±0.24	0.15
G019.0754−00.2874†	19.07543	-0.28737	380.69±37.06	8.49±0.01	333.71±1.81	0.10
G019.4912+00.1352†	19.49123	0.13518	415.07±38.70	11.92±0.01	269.27±1.40	0.34
G019.6087−00.2351†	19.60873	-0.23507	2900.88±260.93	13.11±0.00	855.57±1.90	0.96
G019.6090−00.2313†	19.60899	-0.23126	259.95±26.87	3.84±0.01	126.53±1.91	0.57
G019.7407+00.2821†	19.74069	0.28206	239.01±22.33	17.95±0.02	44.41±2.80	1.32
G019.7549−00.1282†	19.7549	-0.12817	36.52±3.29	1.64±0.03	10.62±0.14	0.97
G020.0720−00.1421†	20.07196	-0.14208	210.13±21.54	5.39±0.01	138.10±1.14	0.33
G020.0789−00.1383†	20.07889	-0.13826	295.86±28.49	19.66±0.03	72.47±1.14	1.11
G020.0809−00.1362	20.0809	-0.13617	498.19±45.06	2.98±0.00	104.42±1.15	1.23±0.07
G020.3633−00.0136†	20.36326	-0.01355	55.11±5.93	2.93±0.01	32.20±1.81	0.42
G021.3571−00.1766	21.35708	-0.17658	24.93±2.34	1.91±0.04	18.49±0.16	0.23±0.07
G021.3855−00.2541	21.38554	-0.25408	113.91±11.24	2.22±0.01	51.09±0.18	0.63±0.08
G021.4257−00.5417†	21.42574	-0.54167	94.85±13.38	10.22±0.04	78.89±0.24	0.14
G023.2654+00.0765†	23.26542	0.07647	88.57±9.87	4.58±0.02	55.58±2.45	0.37
G023.4181−00.3940	23.4181	-0.39403	26.46±2.47	1.77±0.03	18.96±0.21	0.26±0.07
G023.4553−00.2010	23.45526	-0.20096	14.39±1.56	1.71±0.05	2.87±0.47	1.27±0.09
G024.5065−00.2224†	24.50653	-0.22238	205.57±19.72	6.19±0.01	153.69±2.77	0.23
G024.9237+00.0777†	24.92371	0.07769	172.48±20.21	14.93±0.03	57.08±1.87	0.87
G025.3948+00.0332†	25.39478	0.03324	296.86±27.46	4.64±0.01	203.65±2.64	0.30
G025.3970+00.5614	25.39695	0.5614	121.17±11.53	2.04±0.01	93.65±0.68	0.20±0.07
G025.3981−00.1411†	25.39808	-0.14107	2132.24±194.31	8.60±0.01	1351.54±3.30	0.36
G025.7157+00.0487	25.71567	0.04868	20.79±2.96	2.36±0.03	15.67±1.00	0.22±0.11
G025.8011−00.1568	25.80114	-0.15685	31.95±2.96	1.79±0.03	19.20±0.20	0.40±0.07
G026.5444+00.4169†	26.54436	0.4169	413.36±37.39	12.59±0.01	301.02±1.00	0.25
G027.2800+00.1447†	27.27996	0.14468	428.04±42.07	5.75±0.01	370.37±0.25	0.11
G027.3644−00.1657†	27.3644	-0.16574	60.14±6.13	2.26±0.01	44.95±0.21	0.23
G027.9782+00.0789†	27.97822	0.07893	124.00±14.38	9.47±0.03	89.34±1.76	0.26
G028.2879−00.3641†	28.28789	-0.36409	552.77±51.90	4.61±0.01	410.88±0.23	0.23
G029.5780−00.2686†	29.578	-0.26856	6.22±1.00	1.50±0.09	1.98±0.17	0.90
G028.6082+00.0185†	28.6082	0.01854	210.15±20.28	3.62±0.01	168.17±0.29	0.18
G029.9559−00.0168†	29.95585	-0.01677	3116.20±296.94	9.62±0.01	1610.75±1.84	0.52
G030.0096−00.2734	30.00965	-0.27344	4.54±0.94	1.62±0.14	0.3	0.77
G030.5353+00.0204†	30.53526	0.02038	710.36±66.36	6.30±0.01	553.56±0.71	0.20
G030.5887−00.0428†	30.58875	-0.04278	92.37±8.33	1.79±0.03	7.90±0.48	1.93
G030.7197−00.0829†	30.71968	-0.08286	969.33±96.01	4.59±0.01	464.58±2.28	0.58
G030.8662+00.1143†	30.8662	0.11429	325.47±32.96	3.09±0.01	137.17±0.60	0.68
G031.0495+00.4697	31.04949	0.46972	13.64±1.49	1.78±0.06	10.72±0.69	0.19±0.09
G031.2420−00.1106†	31.24202	-0.11062	296.24±27.05	7.81±0.01	174.42±5.67	0.42
G031.1596+00.0448†	31.15958	0.04475	23.83±2.28	1.69±0.04	20.66±0.32	0.11
G031.2801+00.0632†	31.28008	0.06322	268.86±25.67	9.33±0.01	144.48±3.82	0.49
G032.4727+00.2036	32.47274	0.20361	97.38±9.67	2.26±0.01	55.96±0.53	0.44±0.08
G032.7441−00.0755	32.74408	-0.07553	7.93±1.14	1.78±0.10	0.34	1.09
G032.7966+00.1909†	32.79658	0.19091	3123.37±281.38	10.01±0.00	1698.91±2.30	0.48
G032.9273+00.6060†	32.92726	0.60601	285.57±31.27	6.81±0.01	229.50±1.12	0.17
G032.9906+00.0385†	32.99057	0.03852	157.76±18.38	15.24±0.04	102.80±1.07	0.34
G033.1328−00.0923†	33.13277	-0.09228	378.59±34.75	4.02±0.00	173.43±1.43	0.61
G033.4163−00.0036†	33.41627	-0.00358	75.16±9.16	8.78±0.04	57.59±1.61	0.21

Table A1. - *continuum* Information of 120 young positive spectrum HII regions

Name Gal	ℓ (°)	b (°)	$Flux_{5\,GHz}$ (mJy)	Angular diameter (″)	$Flux_{1.4\,GHz}$ (mJy)	Spectral Index
G033.9145+00.1105†	33.9145	0.11045	842.22±88.66	10.14±0.01	464.68±1.90	0.47
G034.2572+00.1535†	34.25724	0.15352	1762.63±163.28	5.75±0.01	370.78±3.39	1.22
G034.4032+00.2277	34.4032	0.22771	8.92±1.24	1.74±0.09	5.27±0.51	0.41±0.11
G035.0242+00.3502	35.02419	0.3502	11.44±1.23	1.55±0.04	5.34±0.40	0.60±0.08
G035.4669+00.1394†	35.46693	0.13942	317.60±29.36	5.12±0.01	235.14±1.11	0.24
G035.5781−00.0305†	35.57813	-0.03048	187.75±18.44	2.53±0.01	38.05±0.97	1.25
G036.4057+00.0226†	36.40568	0.02256	22.34±2.21	1.86±0.05	17.34±1.12	0.20
G037.5457−00.1120†	37.54572	-0.11199	406.46±41.28	8.18±0.01	252.32±1.04	0.37
G037.7347−00.1128	37.73473	-0.11277	16.02±1.63	1.76±0.05	12.27±0.93	0.21±0.08
G037.7633−00.2167†	37.76327	-0.21667	337.64±38.01	14.56±0.03	295.32±2.42	0.11
G037.8731−00.3996†	37.87308	-0.39961	2561.21±234.04	8.92±0.00	1279.35±1.16	0.55
G037.9723−00.0965†	37.97232	-0.09653	20.89±2.52	2.45±0.12	10.22±0.91	0.56
G038.8756+00.3080†	38.87564	0.308	311.31±29.87	3.57±0.01	191.23±1.57	0.38
G039.1956+00.2255	39.19557	0.22546	62.27±6.41	1.95±0.01	14.19±2.24	1.16±0.08
G039.7277−00.3973†	39.72773	-0.39732	133.30±18.10	15.94±0.05	112.30±1.65	0.13
G039.8824−00.3460†	39.88236	-0.34602	276.87±26.38	3.81±0.01	246.97±1.45	0.09
G042.4345−00.2605†	42.43453	-0.26049	83.65±9.25	3.63±0.02	38.47±2.08	0.61
G043.1651−00.0283†	43.1651	-0.02828	2714.29±262.82	9.61±0.01	564.34±8.16	1.23
G043.1665+00.0106†	43.16648	0.01057	1365.68±125.16	3.68±0.00	237.81±8.09	1.37
G043.1778−00.5181†	43.17775	-0.51806	181.65±23.04	7.16±0.03	122.91±1.30	0.31
G045.0694+00.1323†	45.06939	0.1323	46.17±4.44	1.96±0.04	17.93±1.47	0.74
G045.0712+00.1321†	45.07116	0.13206	146.67±14.65	1.89±0.01	61.6±0.6	0.68
G045.1223+00.1321†	45.12233	0.13206	2984.27±274.33	7.46±0.00	1345.96±1.67	0.63
G045.4545+00.0591†	45.4545	0.05908	1029.45±98.24	7.61±0.01	492.46±3.21	0.58
G045.4656+00.0452	45.46557	0.04515	62.26±5.79	1.70±0.03	28.88±1.32	0.60±0.07
G045.4790+00.1294†	45.47896	0.12942	504.23±58.87	13.72±0.03	380.22±3.59	0.22
G048.6057+00.0228	48.60569	0.02278	36.16±3.59	1.74±0.04	6.61±1.05	1.33±0.08
G048.6099+00.0270†	48.60992	0.02697	131.22±15.55	7.06±0.03	56.49±1.07	0.66
G048.9296−00.2793†	48.92959	-0.27926	185.39±19.22	6.16±0.02	66.90±3.92	0.80
G049.2679−00.3374	49.26792	-0.33743	102.61±14.03	6.22±0.50	64.41±1.51	0.37±0.11
G049.3704−00.3012†	49.37036	-0.30117	414.43±47.36	4.68±0.24	252.86±8.37	0.39
G049.4905−00.3688†	49.49053	-0.36881	3821.72±365.24	5.76±0.01	1165.61±5.68	0.93
G050.0457+00.7683	50.04574	0.76833	15.57±1.55	2.04±0.05	13.03±0.39	0.14±0.08
G050.3152+00.6762	50.31525	0.67623	81.31±8.07	2.11±0.01	38.74±2.01	0.58±0.08
G050.3157+00.6747†	50.31566	0.67475	73.26±8.30	9.82±0.03	15.88±1.99	1.20
G051.6785+00.7193	51.67854	0.71934	22.55±2.07	1.79±0.03	2.8	0.3
G052.7533+00.3340†	52.75329	0.33397	386.03±36.54	8.66±0.01	264.03±2.23	0.30
G053.9589+00.0320†	53.95892	0.03201	46.00±4.73	2.31±0.01	40.78±1.57	0.09
G057.5474−00.2717†	57.54739	-0.27167	233.68±22.99	13.79±0.01	118.26±1.38	0.54
G060.8838−00.1295†	60.88377	-0.12955	292.06±29.15	22.76±0.03	80.89±1.22	1.01
G061.4763+00.0892†	61.47631	0.08921	718.71±64.37	6.54±0.00	252.71±1.40	0.82

These columns contain the name and Galactic coordinate of each source, the flux density and angular diameter of each source at 5 GHz from CORNISH, flux densities at 1.4 GHz from THOR, MAGPIS and White2005, as well as the spectral indices and its errors. Symbol † means that those objects are detected at both 5 GHz and 1.4 GHz with lower limit of the spectral indices as they are extended at 1.4 GHz. Flux densities of some sources at 1.4 GHz with no errors refer to the noise level at 1.4 GHz to the source position, indicating that these sources are only detected at 5 GHz with the lower limits of spectral indices.

Table A2. Information of total 534 positive spectrum radio objects

Name Gal	ℓ (°)	b (°)	$Flux_{5GHz}$ (mJy)	Angular diameter (″)	$Flux_{1.4GHz}$ (mJy)	Spectral Index
G010.3009−00.1477†	10.30088	-0.1477	631.39±59.30	5.45±0.01	426.18±1.98	0.31
G010.3377+01.0601	10.33767	1.06007	10.54±1.22	1.50±0.05	1.15	0.38
G010.4168+00.9356	10.41684	0.93556	14.38±1.51	1.58±0.04	1.3	0.54
G010.4724+00.0275†	10.47236	0.0275	38.43±4.38	2.24±0.02	31.26±0.35	0.16
G010.4727−00.6742†	10.47275	-0.67423	6.28±1.18	1.90±0.16	2.84±0.25	0.62
G010.6223−00.3788†	10.62231	-0.37877	483.33±49.87	5.76±0.01	327.63±1.89	0.31
G010.6234−00.3837†	10.6234	-0.38369	1952.22±176.18	4.64±0.00	571.28±1.88	0.97
G010.6790−00.1668	10.67898	-0.16679	11.09±2.30	3.01±0.36	0.34	1.29
G010.8654−00.8883	10.86538	-0.88834	40.71±3.73	1.53±0.03	31.10±0.95	0.21±0.07
G010.8677−00.0052	10.86766	-0.00519	5.92±1.10	1.79±0.14	0.16	1.41
G010.9584+00.0221†	10.95839	0.02206	195.97±18.33	2.20±0.00	47.92±0.40	1.11
G011.0328+00.0274†	11.03283	0.02738	5.69±1.06	1.89±0.15	3.71±0.28	0.34
G011.1104−00.3985†	11.11043	-0.39851	305.37±28.55	8.36±0.01	253.15±0.42	0.15
G011.1712−00.0662†	11.17121	-0.06621	102.17±12.73	10.75±0.04	83.15±0.32	0.16
G011.2436+01.0526	11.24356	1.05259	11.90±2.62	3.27±0.44	0.37	0.76
G011.3266−00.3718†	11.3266	-0.37184	13.82±2.41	2.77±0.06	10.86±0.29	0.19
G011.4581+01.0736	11.45809	1.07358	7.43±1.15	1.81±0.11	1.12	0.09
G011.9222+01.0978	11.92218	1.09779	6.80±0.88	1.54±0.07	1.08	0.07
G011.9368−00.6158†	11.93677	-0.61577	1155.90±105.38	5.89±0.00	735.63±0.43	0.36
G011.9446−00.0369†	11.94458	-0.03686	943.58±98.50	14.64±0.01	251.14±1.91	1.04
G011.9709+00.1913	11.97091	0.1913	29.50±2.73	1.67±0.03	25.57±0.27	0.11±0.07
G011.9786−00.0973	11.97859	-0.09725	4.46±1.08	1.75±0.19	3.24±0.38	0.25±0.19
G012.0438−00.5077	12.04384	-0.50768	13.49±1.38	1.55±0.04	5.57±0.27	0.69±0.08
G012.1157+00.0757†	12.11571	0.0757	47.37±4.40	2.43±0.05	38.50±2.28	0.16
G012.1528−00.3304	12.15285	-0.33041	11.97±1.42	1.84±0.07	3.33±0.27	1.01±0.09
G012.1772+00.6886	12.17718	0.68858	6.69±1.19	2.01±0.16	0.34	0.91
G012.1988−00.0345†	12.1988	-0.03447	62.71±5.92	2.68±0.06	47.56±0.31	0.22
G012.2081−00.1019†	12.20806	-0.10189	207.87±19.73	2.84±0.01	127.94±1.17	0.38
G012.3315−00.1806†	12.33146	-0.18058	33.65±3.30	2.36±0.06	28.21±0.24	0.14
G012.3830+00.7990	12.38299	0.79904	19.59±1.98	1.70±0.04	11.32±1.33	0.43±0.08
G012.4294−00.0479†	12.4294	-0.04791	45.17±4.35	2.72±0.07	24.39±1.26	0.48
G012.6012+00.5592†	12.60121	0.55923	17.11±1.70	1.57±0.04	5.38±0.23	0.91
G012.8050−00.2007†	12.805	-0.20067	12616.40±1120.83	16.23±0.01	4332.25±4.27	0.84
G012.8131−00.1976†	12.8131	-0.19759	1500.39±147.30	5.43±0.01	907.68±4.18	0.39
G012.8162+00.5576	12.81616	0.5576	11.82±1.32	1.50±0.05	8.82±1.36	0.23±0.09
G012.9995−00.3583†	12.99951	-0.3583	20.14±3.70	3.09±0.32	10.52±0.28	0.51
G013.2054−00.1089	13.20544	-0.10888	9.28±1.66	2.24±0.19	0.19	1.65
G013.2099−00.1428†	13.20989	-0.14281	946.76±87.46	8.35±0.01	437.88±3.66	0.61
G013.3850+00.0684†	13.38496	0.06835	603.94±60.83	19.18±0.01	139.16±1.16	1.15
G013.7505+00.3195†	13.75054	0.31945	5.49±1.34	1.86±0.21	2.52±0.25	0.61
G013.9166+00.6500	13.91658	0.64998	27.01±2.62	2.04±0.05	15.21±1.35	0.45±0.08
G014.1337+00.0407	14.13369	0.0407	8.95±1.06	1.50±0.05	1.92±0.18	1.21±0.09
G014.7785−00.3328	14.77849	-0.33278	18.25±2.47	2.31±0.03	15.39±1.04	0.13±0.11
G014.8525−01.0925	14.85251	-1.09255	6.25±1.54	1.80±0.20	0.54	0.49
G014.8960+00.4837†	14.89603	0.48373	8.84±1.22	1.61±0.08	7.70±0.22	0.11
G015.3581+00.1342	15.35808	0.13421	4.67±0.94	1.77±0.15	0.3	0.8
G015.5410+00.3359	15.54101	0.33593	21.92±3.22	2.08±0.03	12.28±0.20	0.46±0.12
G015.5847+00.4002	15.58467	0.4002	21.91±2.13	1.66±0.04	10.12±0.28	0.61±0.08
G015.6192+01.1190	15.61918	1.11905	13.63±1.66	1.61±0.06	0.76	1.01
G015.6291+01.1161	15.62907	1.11605	18.16±2.04	1.57±0.05	0.73	1.31
G015.7550−01.0434	15.75499	-1.04344	6.28±0.93	1.50±0.08	0.53	0.62
G015.7993−00.0063†	15.79925	-0.00625	49.17±4.45	1.80±0.03	34.22±0.31	0.28
G015.9917+00.9423	15.99174	0.94232	5.59±1.20	2.29±0.25	4.22±0.24	0.22±0.17
G016.0550+00.8280	16.05504	0.82804	14.13±1.43	1.68±0.04	8.88±1.48	0.36±0.08
G016.1448+00.0088†	16.14482	0.00876	14.76±1.55	1.60±0.04	8.75±0.19	0.41
G016.2951−00.5728	16.29512	-0.57281	3.11±0.75	1.50±0.14	1.22±0.18	0.74±0.19
G016.3913−00.1383†	16.39128	-0.13827	124.27±15.43	11.74±0.04	40.83±0.31	0.87
G016.4708+00.1500†	16.47079	0.15005	33.62±3.05	1.54±0.02	15.93±0.18	0.59
G016.4999+00.1152	16.49986	0.11519	15.78±2.30	3.81±0.30	11.68±0.41	0.24±0.11
G016.6197+00.5979	16.6197	0.59789	3.85±0.82	1.73±0.16	2.66±0.29	0.29±0.17
G016.6995−00.9775	16.69951	-0.97752	4.39±0.83	1.75±0.14	3.26±0.75	0.23±0.15
G016.7598−00.6207†	16.75983	-0.62065	10.69±1.11	1.55±0.04	5.40±0.20	0.54
G016.7821−00.6178	16.78215	-0.61781	44.61±4.00	1.50±0.02	37.82±0.20	0.13±0.07
G016.9445−00.0738†	16.94449	-0.07379	519.34±47.78	3.46±0.00	258.51±0.34	0.55
G016.9471+00.6451	16.94712	0.64512	7.96±1.67	2.68±0.31	6.10±0.61	0.21±0.16
G017.0299−00.0696	17.02987	-0.06955	5.38±1.06	2.39±0.24	1.99±0.37	0.78±0.15
G017.0479+01.0853	17.04787	1.08532	4.77±0.91	1.57±0.12	0.24	1.03
G017.0929+00.5713†	17.09292	0.57131	8.60±1.65	2.68±0.28	5.78±0.13	0.31
G017.1141−00.1124†	17.11407	-0.11236	17.21±2.19	2.83±0.16	14.22±0.25	0.15
G017.2233+00.3952†	17.22333	0.39521	199.86±19.69	3.56±0.01	125.92±0.28	0.36
G017.2304−00.6994	17.2304	-0.69937	2.56±0.60	1.63±0.16	0.24	0.39
G017.3215−00.6936	17.32149	-0.69364	31.54±2.85	1.52±0.02	22.54±0.21	0.26±0.07
G017.3669+00.5224†	17.36686	0.52244	18.42±1.94	2.45±0.08	16.33±0.25	0.09
G017.4147+00.3791†	17.41465	0.37906	41.03±5.11	6.77±0.04	25.53±1.22	0.37
G017.4275+00.2999†	17.42753	0.29993	4.36±0.71	1.50±0.09	2.97±0.20	0.30
G017.4464−00.6615	17.44641	-0.66147	14.39±1.40	1.64±0.04	5.70±0.21	0.73±0.08
G017.7098+00.7672†	17.70978	0.76722	9.13±0.97	1.50±0.04	6.31±0.34	0.29
G017.7794−00.0082	17.77942	-0.00825	4.66±0.70	1.50±0.08	3.38±0.26	0.25±0.12
G017.7975+00.0570	17.79746	0.05704	8.62±0.91	1.50±0.04	6.03±0.39	0.28±0.08
G017.8222+00.9866	17.82218	0.98658	15.37±1.76	2.43±0.10	11.70±0.75	0.21±0.09

Table A2. -continuum Information of total 534 positive spectrum radio objects

Name Gal	ℓ (°)	b (°)	Flux$_{5GHz}$ (mJy)	Angular diameter (″)	Flux$_{1.4GHz}$ (mJy)	Spectral Index
G017.8409−00.1765†	17.8409	-0.17647	6.58±0.82	1.64±0.07	3.77±0.21	0.44
G017.8645+00.2120†	17.86448	0.21199	23.35±2.16	1.57±0.03	6.97±0.20	0.95
G017.9275+00.6337	17.92751	0.63366	4.40±0.71	1.50±0.09	0.1	1.56
G018.0661+00.8535	18.0661	0.85354	33.16±3.24	2.83±0.08	20.09±1.33	0.39±0.08
G018.1286−00.2189†	18.12862	-0.2189	8.54±1.70	1.95±0.18	5.17±0.36	0.39
G018.1460−00.2839†	18.14602	-0.2839	856.18±82.85	23.42±0.02	151.22±1.93	1.36
G018.2218−00.9806	18.22177	-0.98056	2.69±0.61	1.50±0.13	0.34	0.18
G018.2402−00.9152†	18.24021	-0.91519	65.18±8.31	8.08±0.03	46.11±0.76	0.27
G018.2413−00.5552	18.24127	-0.55516	8.24±0.91	1.50±0.05	1.45±0.17	1.36±0.09
G018.3024−00.3910†	18.30241	-0.39103	1277.88±114.83	14.63±0.00	846.82±0.32	0.32
G018.3958+00.0500	18.39576	0.04997	9.34±1.06	1.77±0.06	7.10±0.22	0.22±0.09
G018.4433−00.0056†	18.44328	-0.00558	81.31±7.30	2.41±0.04	56.18±0.37	0.29
G018.4614−00.0038†	18.46141	-0.00378	342.12±31.50	2.76±0.00	128.20±0.47	0.77
G018.4719+00.3401	18.47192	0.34012	16.87±1.60	1.56±0.03	6.20±0.20	0.79±0.07
G018.4887+00.8996	18.48867	0.89959	51.15±4.57	1.50±0.02	21.18±0.25	0.69±0.07
G018.5073−00.9692	18.50726	-0.96917	3.22±0.60	1.50±0.10	0.24	0.69
G018.5242+00.1519	18.52417	0.1519	3.65±0.78	1.76±0.16	0.15	1.64
G018.5473+00.7354†	18.54726	0.73539	11.88±1.20	1.50±0.04	5.12±0.26	0.66
G018.5776−00.7484	18.57761	-0.74837	7.60±1.50	2.83±0.31	5.29±0.23	0.28±0.16
G018.6654+00.0294	18.66539	0.02935	5.65±0.85	1.74±0.10	3.74±0.21	0.32±0.12
G018.7086−00.1265†	18.70864	-0.12646	144.26±13.96	2.08±0.01	51.48±0.31	0.81
G018.7106+00.0002	18.71061	2.2E-4	107.46±10.62	2.04±0.01	40.95±0.31	0.76±0.08
G018.7612+00.2630†	18.76118	0.26298	51.38±4.67	1.79±0.03	26.45±0.23	0.52
G018.8250−00.4675†	18.82499	-0.46749	11.41±2.17	2.53±0.25	9.08±0.35	0.18
G018.8338−00.3002†	18.83384	-0.30024	131.38±13.35	6.72±0.01	108.41±0.24	0.15
G018.8778+00.2282†	18.87777	0.22818	5.41±0.79	1.61±0.09	2.20±0.17	0.71
G018.9195−01.0872	18.91952	-1.0872	7.34±1.46	2.19±0.21	0.28	1.26
G019.0225+01.0444	19.02251	1.0444	9.20±1.10	1.63±0.06	6.40±1.07	0.29±0.09
G019.0578+00.4045	19.05781	0.40452	4.55±0.81	1.73±0.12	0.19	1.21
G019.0754−00.2874†	19.07543	-0.28737	380.69±37.06	8.49±0.01	333.71±1.81	0.10
G019.0929+01.0389	19.09287	1.03892	4.10±0.96	1.61±0.16	0.21	0.98
G019.1240+00.9057	19.12404	0.9057	5.12±0.86	1.66±0.11	3.68±0.29	0.26±0.13
G019.2024−00.5677†	19.20241	-0.56766	4.60±0.85	1.87±0.15	1.49±0.15	0.89
G019.3528−00.6566	19.35282	-0.6566	5.99±0.77	1.56±0.07	2.24±0.21	0.77±0.10
G019.4676−00.0154	19.46763	-0.01544	18.81±1.85	1.85±0.04	12.98±0.50	0.29±0.08
G019.4912+00.1352†	19.49123	0.13518	415.07±38.70	11.92±0.01	269.27±1.40	0.34
G019.5326+00.7308	19.53258	0.73085	5.97±1.12	1.97±0.17	4.94±0.27	0.15±0.15
G019.5814−00.5818	19.58145	-0.58185	4.73±0.74	1.78±0.11	3.78±0.16	0.18±0.12
G019.6087−00.2351†	19.60873	-0.23507	2900.88±260.93	13.11±0.00	855.57±1.90	0.96
G019.6090−00.2313†	19.60899	-0.23126	259.95±26.87	3.84±0.01	126.53±1.91	0.57
G019.6845+00.8479	19.68451	0.84786	2.32±0.68	1.50±0.18	0.96±0.15	0.69±0.23
G019.7407+00.2821†	19.74069	0.28206	239.01±22.33	17.95±0.02	44.41±2.80	1.32
G019.7549−00.1282†	19.7549	-0.12817	36.52±3.29	1.64±0.03	10.62±0.14	0.97
G019.8662−00.3575†	19.8662	-0.35751	6.35±1.35	2.55±0.29	2.70±0.14	0.67
G019.9298−00.6639	19.92975	-0.66392	14.12±1.38	1.50±0.03	6.33±0.16	0.63±0.08
G019.9427+00.7581	19.94269	0.75809	30.11±2.73	1.50±0.02	10.79±1.70	0.81±0.07
G019.9448+00.9126	19.94476	0.91259	29.79±3.07	2.49±0.08	26.69±1.07	0.09±0.08
G020.0720−00.1421†	20.07196	-0.14208	210.13±21.54	5.39±0.01	138.10±1.14	0.33
G020.0789−00.1383†	20.07889	-0.13826	295.86±28.49	19.66±0.03	72.47±1.14	1.11
G020.0809−00.1362	20.0809	-0.13617	498.19±45.06	2.98±0.00	104.42±1.15	1.23±0.07
G020.1612+00.4510	20.16122	0.45097	14.94±1.49	1.56±0.04	12.53±0.15	0.14±0.08
G020.1737+01.0951	20.17367	1.09508	4.39±1.23	1.50±0.17	0.24	0.85
G020.1859−01.0369	20.1859	-1.03686	6.86±0.86	1.61±0.07	3.15±0.24	0.61±0.10
G020.3633−00.0136†	20.36326	-0.01355	55.11±5.93	2.93±0.01	32.20±1.81	0.42
G020.3781−00.2144†	20.37808	-0.21438	7.30±0.92	1.50±0.06	4.68±0.16	0.35
G020.4092+00.0996	20.40923	0.09961	4.21±0.98	1.76±0.18	2.75±0.44	0.33±0.18
G020.4681+00.6793†	20.46809	0.67926	86.39±8.66	2.64±0.01	71.13±0.17	0.15
G020.5899+00.6569	20.58987	0.65692	4.61±0.74	1.50±0.09	3.74±0.18	0.16±0.13
G020.6457−00.6833	20.64572	-0.68328	11.02±1.16	1.55±0.04	8.96±0.28	0.16±0.08
G020.6568−00.9640	20.65678	-0.96399	6.40±1.44	2.18±0.25	0.29	1.08
G020.7212+00.1054	20.72117	0.10542	3.05±0.77	1.58±0.17	0.23	0.55
G020.7989+00.1225	20.79888	0.1225	16.97±1.61	1.55±0.03	10.70±0.13	0.36±0.07
G020.8085+00.3700	20.80847	0.37004	15.40±1.46	1.50±0.03	13.84±0.17	0.08±0.07
G020.8133+00.4323†	20.81328	0.4323	3.48±0.82	1.67±0.17	2.46±0.17	0.27
G020.8967−01.0373	20.89671	-1.0373	5.15±0.78	1.50±0.08	1.98±0.32	0.75±0.12
G020.9782+00.9253	20.97815	0.92531	13.72±1.88	2.61±0.16	10.51±1.16	0.21±0.11
G021.1653+00.4755	21.16525	0.47554	131.71±12.41	1.98±0.00	48.51±0.15	0.78±0.07
G021.3076+00.0835	21.30762	0.08351	4.16±1.04	1.84±0.21	0.16	1.18
G021.3155−00.1625	21.3155	-0.16251	5.35±1.13	2.31±0.25	3.99±0.31	0.23±0.17
G021.3402−01.0880	21.34025	-1.08801	40.70±3.85	1.58±0.03	0.23	3.03
G021.3425−00.8423†	21.34254	-0.84231	17.57±2.72	2.04±0.14	6.03±0.62	0.84
G021.3474−00.6294	21.34739	-0.62939	1318.01±118.33	1.67±0.00	1057.73±0.30	0.17±0.07
G021.3571−00.1766	21.35708	-0.17658	24.93±2.34	1.91±0.04	18.49±0.16	0.23±0.07
G021.3855−00.2541	21.38554	-0.25408	113.91±11.24	2.22±0.01	51.09±0.18	0.63±0.08
G021.4257−00.5417†	21.42574	-0.54167	94.85±13.38	10.22±0.04	78.89±0.24	0.14
G021.6221−00.7422	21.62208	-0.74224	21.17±1.95	1.50±0.03	5.41±0.23	1.07±0.07
G021.6553−00.3612	21.65526	-0.36117	54.68±4.89	1.50±0.02	26.00±0.20	0.58±0.07
G021.6657+00.8110	21.66567	0.81095	52.92±4.76	1.69±0.03	13.01±1.21	1.10±0.07
G021.7639+00.9012	21.76395	0.90123	6.85±0.94	1.58±0.07	3.59±0.29	0.51±0.11
G021.8201−00.4779	21.82009	-0.47787	34.20±3.93	3.77±0.18	29.64±0.78	0.11±0.09

Table A2. -continuum Information of total 534 positive spectrum radio objects

Name Gal	ℓ (°)	b (°)	Flux$_{5\,GHz}$ (mJy)	Angular diameter (″)	Flux$_{1.4\,GHz}$ (mJy)	Spectral Index
G021.9836+00.7962	21.98358	0.79623	5.53±0.77	1.50±0.07	4.56±0.18	0.15±0.11
G021.9972−00.8838	21.99717	-0.88375	14.22±1.65	2.03±0.08	10.83±0.38	0.21±0.09
G022.1540−00.1542†	22.15397	-0.15417	22.29±2.10	1.70±0.03	16.34±0.18	0.24
G022.1794+00.7537	22.17939	0.75374	39.08±3.51	1.51±0.02	28.17±0.24	0.26±0.07
G022.2211+00.9009	22.22111	0.90093	21.38±2.39	2.46±0.10	14.31±0.77	0.32±0.09
G022.5477−00.1061†	22.54772	-0.10612	32.09±3.03	2.01±0.04	24.94±1.05	0.20
G022.6429−00.4422†	22.6429	-0.4422	6.30±1.16	1.90±0.15	3.66±0.25	0.43
G022.6580+00.2959	22.658	0.29587	14.15±1.42	1.68±0.04	10.64±0.14	0.22±0.08
G023.2654+00.0765†	23.26542	0.07647	88.57±9.87	4.58±0.02	55.58±2.45	0.37
G023.4181−00.3940	23.4181	-0.39403	26.46±2.47	1.77±0.03	18.96±0.21	0.26±0.07
G023.4186+00.0089	23.41864	0.00893	6.27±0.87	1.58±0.08	0.91±0.15	1.51±0.11
G023.4553−00.2010	23.45526	-0.20096	14.39±1.56	1.71±0.05	2.87±0.47	1.27±0.09
G023.5610−00.5920	23.561	-0.59198	9.28±1.06	1.62±0.06	3.57±0.17	0.75±0.09
G023.5635−00.8705	23.56353	-0.87053	5.22±0.74	1.50±0.07	3.00±0.24	0.44±0.11
G023.6645−00.0373	23.66447	-0.03727	26.73±2.44	1.50±0.03	2.49±0.14	1.86±0.07
G023.6893+00.0791	23.68932	0.07913	7.34±1.55	1.76±0.16	0.14	1.64
G023.7074+00.1646†	23.70741	0.16463	667.77±57.61	30.16±0.03	46.54±2.88	2.09
G023.8214−00.5788	23.8214	-0.57885	52.14±4.71	1.86±0.03	29.20±0.14	0.46±0.07
G023.8897−00.7379†	23.88973	-0.73794	113.35±10.72	2.07±0.01	57.97±0.22	0.53
G023.9029+00.5423	23.90293	0.54226	3.42±0.71	1.50±0.13	2.73±0.41	0.18±0.16
G023.9600+01.0543	23.95998	1.05428	5.63±0.80	1.61±0.08	1.60±0.23	0.99±0.11
G024.0943−01.0992	24.09433	-1.09925	16.40±1.55	1.50±0.03	8.62±1.00	0.51±0.07
G024.1659+00.2502†	24.16589	0.25021	36.97±6.77	7.33±0.07	29.44±0.19	0.18 14
G024.3973+00.7938	24.39729	0.79377	6.83±1.03	1.67±0.09	5.44±0.39	0.18±0.12
G024.4513+00.7920	24.45133	0.79201	4.09±0.86	1.68±0.15	2.60±0.47	0.36±0.17
G024.4576−00.1903	24.45759	-0.19031	9.73±1.51	2.01±0.13	6.84±0.61	0.28±0.12
G024.4859+00.6142	24.48592	0.61419	82.56±8.09	1.72±0.01	53.37±2.38	0.34±0.08
G024.5065−00.2224†	24.50653	-0.22238	205.57±19.72	6.19±0.01	153.69±2.77	0.23
G024.5343−00.1020	24.53432	-0.10204	6.54±0.86	1.50±0.06	0.59±0.09	1.88±0.10
G024.5405−00.1378	24.54054	-0.13777	6.22±0.84	1.50±0.07	4.74±0.73	0.21±0.11
G024.6775+00.5493	24.67745	0.54934	75.46±7.57	1.79±0.01	18.38±0.17	1.11±0.08
G024.7921−01.0043	24.79211	-1.00425	9.69±1.39	2.02±0.12	8.39±0.71	0.11±0.11
G024.8959+00.4586†	24.89588	0.45857	13.32±1.95	1.94±0.03	7.17±0.18	0.49
G024.9237+00.0777†	24.92371	0.07769	172.48±20.21	14.93±0.03	57.08±1.87	0.87
G025.0485−00.6621	25.04851	-0.6621	30.11±2.75	1.74±0.03	19.55±0.18	0.34±0.07
G025.1519−00.8656	25.15194	-0.86555	5.82±0.90	1.61±0.09	4.82±0.37	0.15±0.12
G025.3948+00.0332†	25.39478	0.03324	296.86±27.46	4.64±0.01	203.65±2.64	0.30
G025.3970+00.5614	25.39695	0.5614	121.17±11.53	2.04±0.01	93.65±0.68	0.20±0.07
G025.3981−00.1411†	25.39808	-0.14107	2132.24±194.31	8.60±0.01	1351.54±3.30	0.36
G025.5190+00.2165†	25.51899	0.2165	267.32±24.90	7.97±0.01	109.32±3.07	0.70
G025.5198+00.9992	25.5198	0.9992	3.00±0.71	1.79±0.19	0.43	0.05
G025.7157+00.0487	25.71567	0.04868	20.79±2.96	2.36±0.03	15.67±1.00	0.22±0.11
G025.8011−00.1568	25.80114	-0.15685	31.95±2.96	1.79±0.03	19.20±0.20	0.40±0.07
G025.9035+01.0403	25.90345	1.04025	10.94±1.16	1.50±0.04	6.85±0.24	0.37±0.08
G026.0083+00.1369	26.0083	0.13693	6.58±1.03	1.84±0.12	3.26±0.16	0.55±0.12
G026.1302+00.3674	26.13017	0.36743	2.81±0.64	1.50±0.14	1.35±0.20	0.58±0.18
G026.2268+00.7685	26.22684	0.76845	6.46±1.01	1.86±0.12	5.23±0.24	0.17±0.12
G026.4700+00.0209†	26.46996	0.02088	36.46±3.37	1.79±0.03	30.71±0.23	0.13
G026.5444+00.4169†	26.54436	0.4169	413.36±37.39	12.59±0.01	301.02±1.00	0.25
G026.5662+00.2975	26.5662	0.29752	3.64±0.78	1.50±0.12	2.44±0.15	0.31±0.17
G026.6306−00.5756†	26.63062	-0.57564	17.52±1.68	1.50±0.03	13.73±1.13	0.19
G026.7145+00.1319	26.71454	0.13186	13.16±1.51	1.94±0.07	11.56±0.55	0.10±0.09
G026.7627−00.8383	26.76271	-0.83833	12.06±1.27	1.59±0.04	7.45±0.97	0.38±0.08
G026.7872−00.3585	26.78718	-0.35851	4.78±1.11	1.98±0.22	3.54±0.21	0.24±0.18
G026.8304−00.2067	26.83038	-0.20666	12.31±1.51	1.98±0.09	10.21±0.32	0.15±0.10
G026.8377−00.4121	26.83771	-0.41212	12.48±1.33	1.58±0.04	7.45±0.16	0.41±0.08
G026.9481−00.4827	26.94811	-0.48273	8.39±0.98	1.50±0.05	4.51±0.13	0.49±0.09
G026.9698+00.0216	26.96981	0.02161	4.70±0.83	1.60±0.11	3.25±0.42	0.29±0.14
G027.2800+00.1447†	27.27996	0.14468	428.04±42.07	5.75±0.01	370.37±0.25	0.11
G027.3326+00.0227	27.33265	0.02271	6.16±0.84	1.56±0.07	4.56±0.70	0.24±0.11
G027.3644−00.1657†	27.3644	-0.16574	60.14±6.13	2.26±0.01	44.95±0.21	0.23
G027.4884−00.8951	27.48839	-0.89507	3.90±0.80	1.70±0.15	2.97±0.16	0.21±0.16
G027.6023+00.3953	27.60226	0.3953	4.86±1.00	1.76±0.16	2.36±0.45	0.57±0.16
G027.6595−00.3835	27.6595	-0.38351	11.18±1.15	1.50±0.04	3.77±0.14	0.85±0.08
G027.6635−00.8267	27.66354	-0.82672	8.21±0.95	1.67±0.06	5.60±0.20	0.30±0.09
G027.6843−00.1552	27.68426	-0.15519	3.98±0.86	1.78±0.17	2.61±0.15	0.33±0.17
G027.7610−00.3402	27.76103	-0.34024	13.44±1.39	1.59±0.04	9.00±0.17	0.32±0.08
G027.8175+01.0602	27.81747	1.06021	3.49±0.82	1.50±0.14	0.36	0.33
G027.8628−00.7425	27.86279	-0.74253	4.37±0.89	1.85±0.17	1.00±0.18	1.16±0.16
G027.9782+00.0789†	27.97822	0.07893	124.00±14.38	9.47±0.03	89.34±1.76	0.26
G028.1875+00.5047	28.1875	0.50474	2.61±0.64	1.50±0.15	0.12	0.94
G028.2879−00.3641†	28.28789	-0.36409	552.77±51.90	4.61±0.01	410.88±0.23	0.23
G028.3660−00.9640	28.36598	-0.96404	2.92±0.80	1.50±0.17	0.26	0.44
G028.4662−01.0513	28.4662	-1.05134	2.54±0.72	1.50±0.17	0.35	0.05
G028.5077+01.1541	28.50772	1.1541	7.39±1.74	1.57±0.15	0.95	0.15
G028.5690+00.0813	28.569	0.08134	5.34±1.17	2.01±0.21	0.1	1.65
G028.5968−01.0510	28.59675	-1.05099	2.51±0.67	1.50±0.16	0.23	0.41
G028.6082+00.0185†	28.6082	0.01854	210.15±20.28	3.62±0.01	168.17±0.29	0.18
G028.8364−01.1142	28.83645	-1.11417	3.31±0.95	1.73±0.22	0.25	0.55
G028.9064+00.2548	28.90642	0.25482	3.47±0.87	1.50±0.15	0.12	1.14

Table A2. -continuum Information of total 534 positive spectrum radio objects

Name Gal	ℓ (°)	b (°)	Flux$_{5GHz}$ (mJy)	Angular diameter (″)	Flux$_{1.4GHz}$ (mJy)	Spectral Index
G029.1382+00.8332	29.1382	0.83317	13.74±1.46	1.50±0.04	6.36±0.23	0.61±0.08
G029.2555−00.8653	29.25545	-0.86532	3.16±0.81	1.73±0.20	0.39	0.17
G029.2620+00.2916	29.26197	0.29162	2.76±0.75	1.50±0.17	0.13	0.86
G029.3096+00.5124	29.30957	0.51242	2.84±0.70	1.50±0.15	0.12	1.01
G029.4404−00.3199	29.44038	-0.31986	2.81±0.81	1.50±0.18	0.23	0.45
G029.5069−01.1293	29.50689	-1.12928	4.22±1.16	1.60±0.19	0.25	0.79
G029.5780−00.2686†	29.578	-0.26856	6.22±1.00	1.50±0.09	1.98±0.17	0.90
G029.5893+00.5789	29.58929	0.57889	4.49±0.76	1.56±0.10	3.57±0.17	0.18±0.13
G029.7162−00.3179	29.7162	-0.31793	36.01±3.28	1.54±0.03	29.28±0.15	0.16±0.07
G029.7188−00.0316	29.7188	-0.03156	19.09±1.87	1.58±0.04	11.89±0.17	0.37±0.08
G029.7805−00.2661	29.78051	-0.26614	7.53±1.41	2.25±0.21	0.11	1.86
G029.8742−00.8190	29.87424	-0.81897	167.18±16.11	2.19±0.01	69.46±1.27	0.69±0.08
G029.9559−00.0168†	29.95585	-0.01677	3116.20±296.94	9.62±0.01	1610.75±1.84	0.52
G029.9786+00.0206	29.9786	0.02064	6.49±1.12	1.50±0.09	2.74±0.38	0.68±0.14
G029.9822−00.7087	29.98223	-0.70872	3.50±0.89	1.69±0.19	2.60±0.20	0.23±0.20
G030.0096−00.2734	30.00965	-0.27344	4.54±0.94	1.62±0.14	0.3	0.77
G030.0294−00.3318	30.02942	-0.33177	12.97±1.56	1.77±0.07	8.98±0.51	0.29±0.09
G030.0536+00.4411	30.05365	0.44115	4.01±0.93	1.69±0.17	2.55±0.31	0.36±0.18
G030.1039+00.3983	30.10385	0.39828	9.37±1.09	1.50±0.05	6.50±0.31	0.29±0.09
G030.1884+00.1110	30.18837	0.11096	4.45±1.09	1.83±0.20	0.2	0.95
G030.2193+00.6501	30.21926	0.65013	2.80±0.69	1.50±0.15	0.12	1.01
G030.3300+00.0903†	30.33	0.0903	18.59±1.77	1.54±0.03	16.43±0.24	0.10
G030.4377−00.2063†	30.43769	-0.20628	17.72±1.69	1.53±0.03	14.58±0.53	0.15
G030.4461−00.2149	30.4461	-0.21495	8.59±1.05	1.65±0.06	0.2	1.6
G030.4543+00.3223	30.4543	0.32229	3.74±0.88	1.77±0.19	0.1	1.37
G030.5353+00.0204†	30.53526	0.02038	710.36±66.36	6.30±0.01	553.56±0.71	0.20
G030.5887−00.0428†	30.58875	-0.04278	92.37±8.33	1.79±0.03	7.90±0.48	1.93
G030.5966+00.9112	30.59657	0.91115	10.74±1.17	1.57±0.05	4.22±0.36	0.73±0.09
G030.6328−00.7232	30.63283	-0.72321	2.57±0.66	1.50±0.16	0.23	0.41
G030.6670−00.3319†	30.66698	-0.3319	145.92±13.87	1.81±0.00	49.01±0.36	0.86
G030.6881−00.0718†	30.68815	-0.07177	466.99±45.69	10.80±0.03	88.77±4.11	1.30
G030.7197−00.0829†	30.71968	-0.08286	969.33±96.01	4.59±0.01	464.58±2.28	0.58
G030.8000−01.0444	30.79997	-1.04444	3.66±0.82	1.81±0.18	0.29	0.58
G030.8662+00.1143†	30.8662	0.11429	325.47±32.96	3.09±0.01	137.17±0.60	0.68
G030.9254+00.0025†	30.92538	0.00248	13.06±2.62	2.40±0.25	10.37±0.37	0.18
G030.9678−00.6358†	30.96781	-0.63575	9.13±1.40	1.82±0.04	2.74±0.19	0.95
G030.9704−00.7436	30.97042	-0.74359	2.47±0.62	1.50±0.15	0.12	0.88
G030.9715−00.3175	30.97152	-0.31747	3.74±0.74	1.50±0.11	2.87±0.39	0.21±0.16
G030.9924−00.0251	30.99236	-0.02515	3.97±1.02	1.87±0.22	0.12	1.26
G031.0450−00.0949	31.04498	-0.09488	2.63±0.67	1.50±0.15	0.21	0.54
G031.0495+00.4697	31.04949	0.46972	13.64±1.49	1.78±0.06	10.72±0.69	0.19±0.09
G031.0776+00.1703	31.07762	0.17027	6.75±0.93	1.50±0.07	0.22	1.47
G031.1494−00.1728	31.14943	-0.17283	5.18±0.71	1.50±0.07	2.79±0.25	0.49±0.11
G031.1596+00.0448†	31.15958	0.04475	23.83±2.28	1.69±0.04	20.66±0.32	0.11
G031.2131−00.1803	31.21308	-0.18028	2.97±0.67	1.50±0.14	0.27	0.48
G031.2420−00.1106†	31.24202	-0.11062	296.24±27.05	7.81±0.01	174.42±5.67	0.42
G031.2801+00.0632†	31.28008	0.06322	268.86±25.67	9.33±0.01	144.48±3.82	0.49
G031.2859−00.2095	31.28587	-0.20953	3.76±0.93	1.87±0.22	0.11	1.28
G031.3444−00.4625	31.34435	-0.46251	2.78±0.56	1.50±0.12	0.19	0.76
G031.3724−00.7514	31.37238	-0.75138	22.66±2.29	2.16±0.06	17.10±1.96	0.22±0.08
G031.4235−00.9138	31.42349	-0.9138	3.47±0.86	1.71±0.19	0.22	0.76
G031.4704+00.3807	31.4704	0.38071	2.50±0.64	1.50±0.16	0.19	0.52
G031.5694+00.6870	31.56941	0.68699	6.79±0.90	1.50±0.07	5.82±0.23	0.12±0.10
G031.5854−00.0635	31.5854	-0.06353	4.86±0.91	1.72±0.13	3.87±0.20	0.18±0.15
G031.9481+00.7715	31.94808	0.77154	4.38±0.96	1.57±0.14	2.80±0.19	0.35±0.17
G032.2408+00.1667	32.24077	0.16668	3.66±0.86	1.64±0.16	0.16	0.98
G032.2783−00.1705	32.27831	-0.17051	4.80±1.15	1.95±0.22	0.22	0.95
G032.3076+00.1536	32.30764	0.15361	17.67±1.92	1.72±0.05	14.76±0.35	0.14±0.09
G032.3825−00.4869	32.3825	-0.48687	14.24±1.44	1.50±0.04	1.30±0.22	1.88±0.08
G032.4643−00.8749	32.46427	-0.87489	90.42±8.07	1.50±0.02	82.59±0.24	0.07±0.07
G032.4727+00.2036	32.47274	0.20361	97.38±9.67	2.26±0.01	55.96±0.53	0.44±0.08
G032.5485−00.4739	32.54849	-0.47393	51.45±4.71	2.16±0.04	38.29±0.62	0.23±0.07
G032.5996+00.8265	32.59957	0.82652	5.92±0.80	1.50±0.07	3.73±0.39	0.36±0.11
G032.7441−00.0755	32.74408	-0.07553	7.93±1.14	1.78±0.10	0.34	1.09
G032.7635+00.0915	32.76348	0.09148	28.34±2.61	1.53±0.03	10.40±0.61	0.79±0.07
G032.7966+00.1909†	32.79658	0.19091	3123.37±281.38	10.01±0.00	1698.91±2.30	0.48
G032.9273+00.6060†	32.92726	0.60601	285.57±31.27	6.81±0.01	229.50±1.12	0.17
G032.9686−00.4681	32.96862	-0.46807	87.52±7.81	1.50±0.02	52.46±0.38	0.40±0.07
G032.9748+00.2372	32.97478	0.23717	4.59±0.79	1.66±0.11	2.25±0.24	0.56±0.14
G032.9906+00.0385†	32.99057	0.03852	157.76±18.38	15.24±0.04	102.80±1.07	0.34
G033.1328−00.0923†	33.13277	-0.09228	378.59±34.75	4.02±0.00	173.43±1.43	0.61
G033.3526+00.4043	33.35261	0.40435	14.88±1.46	1.56±0.04	6.23±0.47	0.68±0.08
G033.4163−00.0036†	33.41627	-0.00358	75.16±9.16	8.78±0.04	57.59±1.61	0.21
G033.4543−00.6149	33.45434	-0.61491	75.82±6.78	1.76±0.03	19.69±1.07	1.06±0.07
G033.9059−00.0436	33.90593	-0.04363	16.02±1.50	1.53±0.03	2.58±0.22	1.43±0.07
G033.9145+00.1105†	33.9145	0.11045	842.22±88.66	10.14±0.01	464.68±1.90	0.47
G033.9155+00.2639	33.91553	0.2639	3.71±0.95	1.80±0.21	1.54±0.22	0.69±0.20
G033.9622−00.4966	33.96225	-0.49661	2.81±0.67	1.50±0.14	0.3	0.29
G034.1382+00.3805	34.13821	0.38049	3.23±0.80	1.67±0.18	0.32	0.49
G034.1777−00.7115	34.17768	-0.7115	17.42±1.63	1.50±0.03	8.03±1.70	0.61±0.07

Table A2. -continuum Information of total 534 positive spectrum radio objects

Name Gal	ℓ (°)	b (°)	Flux$_{5\,GHz}$ (mJy)	Angular diameter (″)	Flux$_{1.4\,GHz}$ (mJy)	Spectral Index
G034.1782+00.2564	34.17819	0.25638	8.02±1.06	1.50±0.06	2.82±0.31	0.82±0.10
G034.2171−00.6886	34.21709	-0.68863	2.37±0.60	1.57±0.17	0.23	0.36
G034.2541+00.3982	34.25414	0.39817	7.98±1.13	1.64±0.08	6.06±0.43	0.22±0.11
G034.2572+00.1535†	34.25724	0.15352	1762.63±163.28	5.75±0.01	370.78±3.39	1.22
G034.2655+00.7195	34.26547	0.71948	6.96±1.10	1.76±0.11	2.38±0.28	0.84±0.12
G034.2830+00.0087	34.28298	0.00872	7.98±1.62	2.31±0.24	0.2	1.63
G034.3110+00.8427	34.31096	0.84267	4.31±1.02	1.69±0.17	3.40±0.23	0.19±0.19
G034.3555−00.0876	34.35547	-0.08758	4.61±1.09	1.86±0.20	0.16	1.31
G034.3852+00.3526	34.38521	0.35259	4.66±0.92	1.64±0.13	0.22	0.96
G034.3896−00.4163	34.38957	-0.41634	5.24±0.79	1.50±0.08	2.82±0.50	0.49±0.12
G034.4032+00.2277	34.4032	0.22771	8.92±1.24	1.74±0.09	5.27±0.51	0.41±0.11
G034.4200−00.3183	34.42004	-0.31826	12.14±1.33	1.59±0.05	5.29±0.63	0.65±0.09
G034.6120+00.4718	34.61196	0.47177	13.31±1.38	1.50±0.04	6.31±1.12	0.59±0.08
G034.7838+00.3346	34.78375	0.33464	3.72±0.79	1.50±0.12	2.81±0.25	0.22±0.17
G034.8624−00.0630†	34.86237	-0.06301	64.67±7.25	3.40±0.02	37.30±1.11	0.43
G035.0242+00.3502	35.02419	0.3502	11.44±1.23	1.55±0.04	5.34±0.40	0.60±0.08
G035.0605+00.6208	35.06054	0.62084	2.76±0.72	1.50±0.16	0.29	0.29
G035.1378−00.7622†	35.13777	-0.76224	201.82±21.72	15.17±0.03	144.45±1.72	0.26
G035.2136+00.3628	35.21363	0.3628	5.31±0.89	1.50±0.09	1.95±0.27	0.79±0.13
G035.2618+00.1079	35.26179	0.10791	2.36±0.67	1.50±0.17	0.32	0.05
G035.4669+00.1394†	35.46693	0.13942	317.60±29.36	5.12±0.01	235.14±1.11	0.24
G035.4719−00.4365†	35.47194	-0.43652	207.07±19.59	2.81±0.01	141.31±0.95	0.30
G035.5485+00.7199	35.54845	0.71988	4.07±0.72	1.50±0.10	3.25±0.17	0.18±0.14
G035.5781−00.0305	35.57813	-0.03048	187.75±18.44	2.53±0.01	38.05±0.97	1.25±0.08
G035.7340+01.0506	35.73398	1.05064	2.49±0.62	1.50±0.15	0.16	0.75
G035.8491+00.3278	35.84905	0.32782	26.36±2.41	1.53±0.03	17.42±1.87	0.33±0.07
G035.8978+01.0671	35.89785	1.06713	4.49±0.98	1.75±0.17	3.32±0.24	0.24±0.17
G035.9464+00.3787	35.9464	0.37873	176.03±16.35	1.65±0.00	131.21±1.26	0.23±0.07
G036.0116−00.2562	36.01164	-0.25619	18.18±1.70	1.66±0.03	10.48±0.21	0.43±0.07
G036.0591+01.0444	36.05905	1.04443	3.76±0.59	1.50±0.09	0.2	1.02
G036.0890+01.0965	36.08897	1.09646	3.97±0.96	1.50±0.14	0.2	0.97
G036.1445−00.4505	36.1445	-0.45048	3.97±0.71	1.50±0.11	2.91±0.21	0.24±0.14
G036.4057+00.0226†	36.40568	0.02256	22.34±2.21	1.86±0.05	17.34±1.12	0.20
G036.4732+00.2343	36.47315	0.23432	2.54±0.65	1.63±0.18	0.17	0.64
G036.5146−00.8339	36.51461	-0.83394	2.69±0.63	1.50±0.14	1.39±0.15	0.52±0.18
G036.6518+00.9973	36.65176	0.99729	6.37±0.93	1.50±0.08	3.48±0.20	0.47±0.11
G036.6816−00.7292	36.68162	-0.72916	8.52±0.98	1.56±0.05	3.62±0.18	0.67±0.09
G036.6975−00.6303	36.69752	-0.6303	148.75±13.24	1.50±0.02	72.62±1.66	0.56±0.07
G036.7454+00.3202	36.7454	0.32019	5.79±0.85	1.50±0.08	1.40±0.18	1.12±0.12
G036.7774−00.3224	36.77736	-0.32237	2.98±0.77	1.58±0.17	0.34	0.2
G037.0193−00.2896	37.01933	-0.28959	3.16±0.82	1.70±0.19	0.2	0.66
G037.0484−00.0118	37.0484	-0.01176	3.56±0.82	1.64±0.16	0.27	0.55
G037.0531−00.1323	37.05313	-0.13227	4.73±0.96	1.74±0.15	3.62±0.28	0.21±0.16
G037.1398−01.0988	37.13983	-1.09883	8.08±1.03	1.58±0.07	4.19±0.18	0.52±0.10
G037.2384−00.1189	37.23839	-0.11894	3.15±0.75	1.50±0.14	0.31	0.35
G037.2781−00.2259†	37.27811	-0.22591	49.47±7.36	5.68±0.05	28.40±2.58	0.44
G037.3010−00.7520	37.301	-0.75196	19.49±1.80	1.50±0.03	5.16±0.23	1.04±0.07
G037.3865+00.3109	37.38654	0.31094	3.24±0.81	1.57±0.16	0.23	0.59
G037.4611+00.8646	37.46115	0.86459	3.43±0.93	1.80±0.23	0.25	0.59
G037.5457−00.1120†	37.54572	-0.11199	406.46±41.28	8.18±0.01	252.32±1.04	0.37
G037.6436−01.1068	37.64363	-1.10677	2.38±0.52	1.50±0.13	0.2	0.56
G037.6463−01.1079	37.64634	-1.10786	2.20±0.51	1.50±0.14	0.2	0.46
G037.6982+00.6123	37.69818	0.61232	2.66±0.67	1.50±0.15	0.22	0.53
G037.7347−00.1128	37.73473	-0.11277	16.02±1.63	1.76±0.05	12.27±0.93	0.21±0.08
G037.7633−00.2167†	37.76327	-0.21667	337.64±38.01	14.56±0.03	295.32±2.42	0.11
G037.8132−00.9042	37.81322	-0.90422	2.85±0.69	1.50±0.15	0.23	0.57
G037.8671+00.2936	37.86713	0.29355	4.23±0.85	1.63±0.13	2.44±0.27	0.43±0.16
G037.8731−00.3996†	37.87308	-0.39961	2561.21±234.04	8.92±0.00	1279.35±1.16	0.55
G037.8843−01.1146	37.88432	-1.11464	5.02±0.64	1.50±0.06	0.41	0.66
G037.9031−00.2754	37.90313	-0.27535	32.54±2.99	1.64±0.03	14.98±0.39	0.61±0.07
G037.9601+00.4534	37.96014	0.45343	22.68±2.11	1.60±0.03	8.37±0.31	0.78±0.07
G037.9723−00.0965†	37.97232	-0.09653	20.89±2.52	2.45±0.12	10.22±0.91	0.56
G038.5500−00.7381	38.54998	-0.7381	12.07±1.29	1.50±0.04	6.77±0.39	0.45±0.08
G038.8756+00.3080†	38.87564	0.308	311.31±29.87	3.57±0.01	191.23±1.57	0.38
G039.1956+00.2255	39.19557	0.22546	62.27±6.41	1.95±0.01	14.19±2.24	1.16±0.08
G039.2450−00.0673†	39.245	-0.06731	420.86±35.81	27.19±0.03	91.31±1.37	1.20
G039.4191−00.7606	39.41913	-0.76062	17.01±1.59	1.50±0.03	12.91±0.45	0.22±0.07
G039.7277−00.3973†	39.72773	-0.39732	133.30±18.10	15.94±0.05	112.30±1.65	0.13
G039.8824−00.3460†	39.88236	-0.34602	276.87±26.38	3.81±0.01	246.97±1.45	0.09
G040.6282+00.0529	40.62822	0.05291	202.42±18.04	1.50±0.02	90.06±1.09	0.64±0.07
G041.1125+00.0360	41.11251	0.03597	8.97±1.03	1.62±0.06	2.47±0.26	1.01±0.09
G041.1982+00.0348†	41.19816	0.0348	37.90±4.42	2.25±0.02	29.58±1.30	0.19
G041.3540+00.5390	41.35404	0.53897	33.90±3.45	2.78±0.09	27.73±1.12	0.16±0.08
G041.7871+00.4884	41.78711	0.4884	8.23±1.02	1.60±0.06	0.27	1.32
G042.0785+00.5083	42.07851	0.50833	9.32±1.36	2.09±0.13	2.98±0.32	0.90±0.11
G042.4345−00.2605†	42.43453	-0.26049	83.65±9.25	3.63±0.02	38.47±2.08	0.61
G042.4728+00.7421	42.47284	0.7421	67.36±6.02	1.50±0.02	28.29±0.69	0.68±0.07
G042.6034+00.6557	42.6034	0.65567	8.98±1.11	1.62±0.06	5.24±0.49	0.42±0.10
G043.0281+00.1399	43.02813	0.13986	109.64±9.81	2.09±0.03	59.73±0.68	0.48±0.07
G043.1651−00.0283†	43.1651	-0.02828	2714.29±262.82	9.61±0.01	564.34±8.16	1.23

Table A2. -continuum Information of total 534 positive spectrum radio objects

Name Gal	ℓ (°)	b (°)	Flux$_{5\,GHz}$ (mJy)	Angular diameter (″)	Flux$_{1.4\,GHz}$ (mJy)	Spectral Index
G043.1665+00.0106†	43.16648	0.01057	1365.68±125.16	3.68±0.00	237.81±8.09	1.37
G043.1778−00.5181†	43.17775	-0.51806	181.65±23.04	7.16±0.03	122.91±1.30	0.31
G043.1845−00.5268†	43.1845	-0.52684	352.51±37.69	18.96±0.03	306.10±1.33	0.11
G043.2946−00.6455†	43.29464	-0.64553	68.05±6.11	1.81±0.03	26.64±1.80	0.74
G043.5793+00.0261	43.57932	0.02608	16.00±1.52	1.55±0.03	8.94±0.35	0.46±0.07
G043.8056−00.7210	43.80561	-0.72096	13.37±1.33	1.59±0.04	10.94±2.80	0.16±0.08
G044.6375+00.4827	44.63754	0.48266	17.45±1.89	1.94±0.06	10.05±1.10	0.43±0.09
G044.9646+00.2841	44.96459	0.28414	13.62±1.51	1.68±0.05	9.65±0.30	0.27±0.09
G045.0694+00.1323†	45.06939	0.1323	46.17±4.44	1.96±0.04	17.93±1.47	0.74
G045.0712+00.1321†	45.07116	0.13206	146.67±14.65	1.89±0.01	61.6±0.6	0.68
G045.1223+00.1321†	45.12233	0.13206	2984.27±274.33	7.46±0.00	1345.96±1.67	0.63
G045.2830−00.6278	45.28297	-0.62781	21.44±2.22	1.96±0.06	10.45±1.64	0.56±0.08
G045.3657−00.2193	45.36567	-0.21927	143.53±12.79	1.54±0.02	9.59±0.50	2.13±0.07
G045.4545+00.0591†	45.4545	0.05908	1029.45±98.24	7.61±0.01	492.46±3.21	0.58
G045.4656+00.0452	45.46557	0.04515	62.26±5.79	1.70±0.03	28.88±1.32	0.60±0.07
G045.4790+00.1294†	45.47896	0.12942	504.23±58.87	13.72±0.03	380.22±3.59	0.22
G046.0603+00.7280	46.0603	0.72798	28.02±2.56	1.52±0.03	12.63±1.77	0.63±0.07
G046.0717+00.0697	46.07175	0.06968	19.36±1.83	1.50±0.03	16.86±1.01	0.11±0.07
G047.0251−00.4864	47.02513	-0.48635	6.86±1.02	1.50±0.08	5.27±0.89	0.21±0.12
G047.1193+00.6253	47.11933	0.62533	3.51±0.78	1.50±0.13	2.60±0.26	0.24±0.17
G047.2232−00.9768	47.22322	-0.97682	11.22±1.12	1.50±0.04	8.79±0.20	0.19±0.08
G047.3360+01.0083	47.33603	1.0083	4.66±0.71	1.50±0.08	2.14±0.25	0.61±0.12
G047.3423−00.9310	47.34226	-0.931	17.18±1.67	1.50±0.03	14.10±0.18	0.16±0.08
G047.4242+00.7676	47.42423	0.76764	2.44±0.68	1.50±0.17	0.28	0.21
G047.5104+00.1156	47.51043	0.11557	2.17±0.68	1.50±0.19	0.19	0.41
G047.6278+00.9883	47.62782	0.98828	11.37±1.18	1.50±0.04	5.75±0.21	0.54±0.08
G047.6884−00.3024	47.68842	-0.30236	16.41±1.64	1.57±0.04	2.61±0.14	1.44±0.08
G047.9729−00.8876	47.9729	-0.88759	9.51±1.10	1.50±0.05	4.95±0.18	0.51±0.09
G047.9835+01.0508	47.9835	1.05083	3.70±0.81	1.65±0.15	0.68±0.10	1.33±0.17
G047.9953−01.0084	47.99529	-1.00845	3.44±0.86	1.59±0.17	0.95±0.15	1.01±0.20
G048.1015−00.0822	48.10152	-0.0822	3.17±0.83	1.59±0.18	1.81±0.16	0.44±0.21
G048.2632+00.0172	48.26323	0.01723	23.25±2.16	1.50±0.03	12.02±1.44	0.52±0.07
G048.3371+00.1576	48.33714	0.15763	3.84±0.90	1.81±0.19	2.92±0.22	0.22±0.18
G048.3841+00.7889	48.38409	0.78893	121.99±10.87	1.50±0.02	74.56±0.18	0.39±0.07
G048.4709+00.6499	48.47093	0.64986	7.21±0.94	1.50±0.07	4.31±0.17	0.40±0.10
G048.4923−00.0641	48.49231	-0.06407	37.92±4.45	1.81±0.02	25.20±0.96	0.32±0.09
G048.5444−00.0024	48.54438	-0.00239	132.74±11.84	1.51±0.02	77.32±0.94	0.42±0.07
G048.5619+00.9029	48.56189	0.90289	3.56±0.66	1.79±0.14	1.81±0.20	0.53±0.15
G048.6057+00.0228	48.60569	0.02278	36.16±3.59	1.74±0.04	6.61±1.05	1.33±0.08
G048.6099+00.0270†	48.60992	0.02697	131.22±15.55	7.06±0.03	56.49±1.07	0.66
G048.7319+00.9305	48.73194	0.93047	18.62±1.85	1.90±0.05	16.37±0.21	0.10±0.08
G048.7478+00.8645	48.74775	0.86447	3.68±0.59	1.58±0.09	2.35±0.18	0.35±0.13
G048.8229+00.5618	48.82285	0.56184	2.04±0.46	1.50±0.13	1.01±0.17	0.55±0.18
G048.8284+00.2244	48.82843	0.22443	5.49±0.78	1.59±0.08	3.26±0.43	0.41±0.11
G048.9296−00.2793†	48.92959	-0.27926	185.39±19.22	6.16±0.02	66.90±3.92	0.80 08
G049.1196−00.2318	49.11957	-0.23176	18.65±1.80	1.50±0.03	12.52±1.13	0.31±0.08
G049.2679−00.3374	49.26792	-0.33743	102.61±14.03	6.22±0.50	64.41±1.51	0.37±0.11
G049.3704−00.3012†	49.37036	-0.30117	414.43±47.36	4.68±0.24	252.86±8.37	0.39
G049.3848+00.1846	49.38477	0.1846	8.15±0.91	1.58±0.05	5.95±0.46	0.25±0.09
G049.4290−00.0313	49.42898	-0.03129	4.10±0.62	1.50±0.08	0.44	0.41
G049.4905−00.3688†	49.49053	-0.36881	3821.72±365.24	5.76±0.01	1165.61±5.68	0.93
G049.6617−00.0543	49.66172	-0.05429	9.99±1.01	1.50±0.04	8.50±0.66	0.13±0.08
G049.6948+00.8642	49.69479	0.86425	26.55±2.44	1.74±0.03	19.99±0.19	0.22±0.07
G049.7289−00.3647	49.72887	-0.36469	11.37±1.76	2.54±0.19	0.35	1.49
G049.8581+00.1327	49.85809	0.13265	135.47±12.07	1.50±0.02	121.70±1.61	0.08±0.07
G050.0003+00.5072	50.00028	0.50715	19.51±1.85	1.75±0.04	13.95±0.29	0.26±0.07
G050.0208+00.5874	50.02077	0.58738	2.38±0.52	1.50±0.13	0.19	0.57
G050.0457+00.7683	50.04574	0.76833	15.57±1.55	2.04±0.05	13.03±0.39	0.14±0.08
G050.0937+00.3445	50.09372	0.34448	2.70±0.55	1.50±0.12	0.17	0.83
G050.1052+00.1298	50.10517	0.12975	5.39±0.72	1.59±0.07	0.16	1.55
G050.1186+00.3814	50.1186	0.3814	5.89±0.73	1.50±0.06	4.07±0.33	0.29±0.10
G050.1704−00.5746	50.17038	-0.57461	7.47±0.80	1.50±0.04	3.92±0.46	0.51±0.08
G050.2114−00.8858	50.21142	-0.88581	2.80±0.53	1.50±0.11	0.4	0.11
G050.2298+00.3139†	50.22979	0.31385	74.17±11.03	11.46±0.05	60.93±2.70	0.15
G050.2325+00.3342†	50.23251	0.33421	91.84±12.13	11.91±0.05	56.04±2.43	0.39
G050.2337+00.3271	50.23373	0.32706	571.18±50.84	1.50±0.02	484.92±2.52	0.13±0.07
G050.2491−00.4767	50.24914	-0.47673	3.85±0.59	1.50±0.09	2.76±0.49	0.26±0.12
G050.3152+00.6762	50.31525	0.67623	81.31±8.07	2.11±0.01	38.74±2.01	0.58±0.08
G050.3157+00.6747†	50.31566	0.67475	73.26±8.30	9.82±0.03	15.88±1.99	1.20
G050.3420+00.6779	50.34202	0.67793	6.74±0.75	1.50±0.05	3.04±0.31	0.63±0.09
G050.4521+00.0691	50.45211	0.06914	6.07±1.13	2.38±0.22	0.1	1.98
G050.4802+00.7056	50.48021	0.70557	7.02±0.82	1.60±0.06	3.23±0.26	0.61±0.09
G050.4884+00.2159	50.48844	0.21587	2.54±0.53	1.50±0.12	0.14	0.91
G050.5556+00.0448	50.5556	0.04475	129.42±12.39	2.74±0.01	85.99±0.98	0.32±0.08
G050.5737+00.6162	50.57368	0.61618	5.16±0.65	1.50±0.06	3.57±0.22	0.29±0.10
G050.5833−00.1473	50.58327	-0.14725	2.50±0.57	1.50±0.13	0.1	1.15
G050.6256−00.0309	50.62557	-0.03095	701.80±62.46	1.50±0.02	474.10±1.12	0.31±0.07
G050.8235+00.2414	50.82349	0.24136	43.15±3.87	1.51±0.02	16.13±2.29	0.77±0.07
G050.8950+00.0572†	50.89503	0.05723	8.96±1.08	1.87±0.08	7.84±1.05	0.10
G050.9842+01.0625	50.9842	1.06248	67.55±6.03	1.52±0.02	55.51±0.62	0.15±0.07
G051.4142+00.7809	51.41424	0.78094	18.46±1.70	1.50±0.03	2.77	0.15

Table A2. -continuum Information of total 534 positive spectrum radio objects

Name Gal	ℓ (°)	b (°)	Flux$_{5\,GHz}$ (mJy)	Angular diameter (″)	Flux$_{1.4\,GHz}$ (mJy)	Spectral Index
G051.5095+00.1686†	51.50955	0.16864	153.38±14.17	7.51±0.01	43.27±1.15	0.99
G051.5869+00.4807	51.58695	0.48073	9.22±0.93	1.50±0.04	0.98	0.41
G051.6785+00.7193	51.67854	0.71934	22.55±2.07	1.79±0.03	2.8	0.3
G051.7134−00.0192	51.71341	-0.01917	9.13±0.91	1.50±0.04	8.13±1.31	0.09±0.08
G051.8062+00.0389	51.80622	0.03893	9.28±0.92	1.50±0.04	1.31	0.19
G051.8341+00.2838	51.83413	0.28378	76.00±6.81	2.25±0.03	54.55±2.00	0.26±0.07
G052.3123+00.1372	52.31232	0.13723	9.73±0.98	1.57±0.04	7.23±1.66	0.23±0.08
G052.6399+00.4864	52.63995	0.48637	18.90±1.74	1.53±0.03	6.74±1.26	0.81±0.07
G052.7533+00.3340†	52.75329	0.33397	386.03±36.54	8.66±0.01	264.03±2.23	0.30
G052.9944−00.6452	52.99438	-0.64517	12.00±1.15	1.50±0.03	9.91±1.09	0.15±0.08
G053.0610−00.4363	53.06104	-0.43628	5.44±0.68	1.50±0.06	0.94	0.01
G053.0922−00.6958	53.0922	-0.69584	16.55±1.54	1.50±0.03	1.46	0.57
G053.2345−00.5657	53.23448	-0.56572	8.70±0.90	1.50±0.04	1.43	0.07
G053.9589+00.0320†	53.95892	0.03201	46.00±4.73	2.31±0.01	40.78±1.57	0.09
G053.9983+00.6941	53.9983	0.69408	74.54±6.65	1.51±0.02	62.91±1.40	0.13±0.07
G055.3753−00.4873	55.37533	-0.48734	6.76±0.74	1.50±0.05	3.39±1.05	0.54±0.09
G055.5070−00.5579	55.50705	-0.55795	203.10±18.69	2.44±0.00	89.81±0.91	0.64±0.07
G055.5083+00.5022	55.50828	0.50218	5.98±0.69	1.50±0.05	0.89	0.14
G055.6596−00.2714	55.65959	-0.27144	36.42±3.27	1.50±0.02	12.32±1.98	0.85±0.07
G057.0097+00.1722	57.00966	0.17223	11.66±1.13	1.50±0.03	1.22	0.43
G057.5474−00.2717†	57.54739	-0.27167	233.68±22.99	13.79±0.01	118.26±1.38	0.54
G058.4338+00.1788	58.43384	0.17879	15.04±1.39	1.50±0.03	7.05±1.27	0.60±0.07
G058.5151−00.4601	58.51507	-0.4601	15.82±1.47	1.53±0.03	11.05±0.90	0.28±0.07
G058.5350−00.4302	58.53496	-0.4302	9.33±0.94	1.50±0.04	0.98	0.42
G058.7670−00.7248	58.76704	-0.72478	17.26±2.39	3.55±0.04	2.77	0.05
G058.8753+00.1435	58.87527	0.14348	8.13±0.82	1.50±0.04	1.31	0.08
G058.9334+00.0625	58.93343	0.06252	13.64±1.28	1.50±0.03	5.87±0.96	0.66±0.07
G058.9598+00.5001	58.95982	0.50015	16.25±1.51	1.58±0.03	14.68±0.89	0.08±0.07
G058.9606+00.5318	58.9606	0.53182	41.93±3.75	1.51±0.02	36.37±0.90	0.11±0.07
G059.5157+00.3728	59.51566	0.37282	8.24±1.34	2.81±0.23	1.05	0.21
G059.8236−00.5361	59.82358	-0.5361	31.61±2.86	1.70±0.03	13.82±1.23	0.65±0.07
G060.3718−00.3553	60.37182	-0.35528	8.63±1.06	2.04±0.09	1.33	0.1
G060.6455−00.2666	60.64554	-0.26656	47.24±4.22	1.51±0.02	30.46±1.86	0.34±0.07
G060.6878−00.3104	60.68781	-0.31038	16.73±1.55	1.50±0.03	2.13	0.28
G060.8042−00.6321†	60.80421	-0.63206	93.54±10.28	13.68±0.04	27.31±1.62	0.97
G060.8831−00.3962	60.88315	-0.39624	40.40±3.62	1.50±0.02	12.53±1.19	0.92±0.07
G060.8838−00.1295†	60.88377	-0.12955	292.06±29.15	22.76±0.03	80.89±1.22	1.01
G061.3730+00.6861	61.373	0.68607	16.38±1.54	1.54±0.03	1.73	0.42
G061.4763+00.0892†	61.47631	0.08921	718.71±64.37	6.54±0.00	252.71±1.40	0.82
G061.5399+00.4666	61.53994	0.4666	7.67±0.81	1.50±0.04	0.92	0.32
G061.5646−00.7147	61.5646	-0.71469	18.66±1.71	1.50±0.03	1.56	0.61
G062.4936−00.2699†	62.49361	-0.26992	20.25±2.08	2.57±0.08	15.16±1.35	0.23
G062.5827+00.1162	62.58267	0.11617	6.97±0.80	1.56±0.05	1.13	0.07
G062.6373−00.3834	62.63729	-0.38338	12.47±1.20	1.50±0.03	1.33	0.42
G062.7551−00.7262	62.75514	-0.72623	16.15±1.65	2.27±0.07	2.74	0.05
G063.4923−00.5914	63.49227	-0.59138	5.81±0.66	1.50±0.05	0.97	0.05
G063.5013+00.4657	63.50128	0.46568	8.77±0.91	1.50±0.04	4.12±0.88	0.59±0.08
G063.6195−00.5529	63.61954	-0.55285	38.25±3.43	1.50±0.02	24.64±1.09	0.35±0.07
G063.8515+00.0716	63.85153	0.07164	37.26±5.00	7.28±0.04	21.57±1.20	0.43±0.11
G063.8893+00.1229†	63.88925	0.12292	33.04±3.94	4.02±0.02	26.35±1.24	0.18
G064.0009−00.7686	64.00087	-0.76856	23.11±2.12	1.50±0.03	1.99	0.59
G064.3305+00.4804	64.33055	0.48039	7.15±0.80	1.57±0.05	1.17	0.06
G064.4590+00.0580	64.45902	0.05799	6.49±0.75	1.61±0.06	0.97	0.14
G065.3071−00.2139	65.30708	-0.21393	988.70±88.00	1.50±0.02	801.03±2.30	0.17±0.07

These columns contain the name and Galactic coordinate of each source, the flux density and angular diameter of each source at 5 GHz from CORNISH, flux densities at 1.4 GHz from THOR, MAGPIS and White2005, as well as the spectral indices and its errors. Symbol † means that those objects are detected at both 5 GHz and 1.4 GHz with lower limit of the spectral indices as they are extended at 1.4 GHz. Flux densities of some sources at 1.4 GHz with no errors refer to the noise level at 1.4 GHz to the source position, indicating that these sources are only detected at 5 GHz with the lower limits of spectral indices.